



ELSEVIER

Contents lists available at ScienceDirect

Journal of Computational Physics

www.elsevier.com/locate/jcp


Eigensolution analysis of spectral/*hp* continuous Galerkin approximations to advection–diffusion problems: Insights into spectral vanishing viscosity



R.C. Moura*, S.J. Sherwin, J. Peiró

Aeronautics Department, Imperial College London, SW7 2AZ, United Kingdom

ARTICLE INFO

Article history:

Received 21 July 2015

Received in revised form 16 November 2015

Accepted 5 December 2015

Available online 11 December 2015

Keywords:

Dispersion–diffusion analysis

Continuous Galerkin formulation

Spectral vanishing viscosity

Stabilization for DNS/LES

ABSTRACT

This study addresses linear dispersion–diffusion analysis for the spectral/*hp* continuous Galerkin (CG) formulation in one dimension. First, numerical dispersion and diffusion curves are obtained for the advection–diffusion problem and the role of multiple eigencurves peculiar to spectral/*hp* methods is discussed. From the eigencurves' behaviour, we observe that CG might feature potentially undesirable non-smooth dispersion/diffusion characteristics for under-resolved simulations of problems strongly dominated by either convection or diffusion. Subsequently, the linear advection equation augmented with spectral vanishing viscosity (SVV) is analysed. Dispersion and diffusion characteristics of CG with SVV-based stabilization are verified to display similar non-smooth features in flow regions where convection is much stronger than dissipation or vice-versa, owing to a dependency of the standard SVV operator on a local Péclet number. First a modification is proposed to the traditional SVV scaling that enforces a globally constant Péclet number so as to avoid the previous issues. In addition, a new SVV kernel function is suggested and shown to provide a more regular behaviour for the eigencurves along with a consistent increase in resolution power for higher-order discretizations, as measured by the extent of the wavenumber range where numerical errors are negligible. The dissipation characteristics of CG with the SVV modifications suggested are then verified to be broadly equivalent to those obtained through upwinding in the discontinuous Galerkin (DG) scheme. Nevertheless, for the kernel function proposed, the full upwind DG scheme is found to have a slightly higher resolution power for the same dissipation levels. These results show that improved CG-SVV characteristics can be pursued via different kernel functions with the aid of optimization algorithms.

© 2015 The Authors. Published by Elsevier Inc. This is an open access article under the CC BY license (<http://creativecommons.org/licenses/by/4.0/>).

1. Introduction

The analysis of dispersion and diffusion errors, both in qualitative and quantitative terms, is a fundamental step in understanding accuracy and stability characteristics of any numerical scheme. This is of particular importance for unstructured high-order methods [1], where the trade-off between small numerical dissipation and robustness for practical problems is a major concern. Not surprisingly, dispersion–diffusion analysis has been applied to several spectral/*hp* methods, such as discontinuous Galerkin [2], spectral volume [3], spectral difference [4] and flux reconstruction [5] schemes. However, to the

* Corresponding author.

E-mail address: rmoura13@imperial.ac.uk (R.C. Moura).

authors' knowledge, this is the first systematic application of eigensolution analysis to the spectral/*hp* continuous Galerkin (CG) formulation. Preliminary studies with related purposes can be found in [6] and [7] (see chapter 6 and references therein). Dispersion–diffusion analyses of the classical (low-order) CG finite element method have also been carried out before, see e.g. [8] for a discussion of element-wise linear and quadratic discretizations.

The one-dimensional linear advection–diffusion equation is considered initially, where the derivation of the discrete problem is described in detail and the dispersion–diffusion curves are evaluated. The role of multiple eigencurves is discussed according to the perspective proposed in [9], where a so-called primary eigencurve is distinguished from the remaining (secondary) ones which are then perceived as replications of the primary curve. An unexpected behaviour of the eigencurves at moderately high wavenumbers is observed for problems strongly dominated by either advection or diffusion, indicating that CG might feature potentially undesirable non-smooth dispersion/diffusion characteristics for such problems, especially in the context of under-resolved simulations. Due to the formulation's lack of numerical dissipation for convection-dominated problems, the effects of spectral vanishing viscosity (SVV) in stabilizing the CG scheme are considered throughout the rest of the paper.

The SVV technique was introduced in [10] in an attempt to stabilize (pure) spectral methods for the simulation of non-linear problems. In a sense, SVV works as a higher-order viscosity because its operator is designed to affect only the highest captured wavenumbers. This feature allows for the exponential (or spectral) convergence property to be preserved for sufficiently resolved simulations. SVV was subsequently adapted for more general spectral methods and applied to the solution of practical engineering problems [11–14]. Moreover, SVV has been used in large-eddy simulations (LES) of turbulent flows playing the role of a turbulence model [13,15–19], even though SVV is not explicitly designed to work as an LES-like subgrid-scale model.

In this paper, the SVV technique is considered as applied to the CG discretization of the linear advection equation in one dimension. The discrete formulation augmented with the standard SVV operator is found, again, to display unusual non-smooth dispersion/diffusion characteristics for problems dominated by either advection or (SVV-based) diffusion. This is due to a dependency on a local Péclet number given by $Pe = ah/\mu$, where a is the advection speed, h is the mesh spacing and μ is the base SVV magnitude. We propose a different approach where the Péclet number is held constant simply by making the base (spectral) viscosity locally proportional to both the advection speed and the mesh spacing, i.e. $\mu \propto ah$. Within this scenario, SVV dissipation is verified to be, in dimensional terms, essentially equivalent to that introduced by upwind fluxes in a discontinuous Galerkin (DG) formulation.

However, while in a DG formulation the wavenumber range where numerical errors are negligible increases with the polynomial order [9], such increase in resolution power is not naturally achieved in CG with SVV-based stabilization. In particular, this is shown for the widely used “exponential” kernel function introduced in [20]. A new SVV kernel function is then proposed which provides a consistent increase in resolution power (as measured by the extent of the wavenumber range where numerical errors are negligible) for higher-order discretizations. Yet, when compared to the (full upwind) DG scheme, the suggested kernel is found to yield a moderately inferior resolution power for the same dissipation levels. We note however that improved CG-SVV characteristics can be pursued via different kernel functions with the aid of optimization algorithms.

This paper is organized as follows. Sec. 2 focuses on the eigen-analysis of the linear advection–diffusion equation with CG, where unexpected behaviours for either advection or diffusion dominated problems are pointed out. Sec. 3 addresses in a similar fashion the advection equation augmented with SVV, discusses the issues with standard SVV operators and proposes a new operator which avoid these issues. In Sec. 4, the equivalence between the proposed SVV approach and upwinding in DG is explored and a comparison of these techniques as applied to CG and DG is carried out. Concluding remarks are given in Sec. 5.

2. Advection–diffusion with CG

This section is devoted to the discretization of the advection–diffusion equation and to the analysis of dispersion and diffusion eigencurves for different polynomial orders. The spectral/*hp* continuous Galerkin method considered closely resembles the formulation presented in [7]. Sec. 2.1 describes in detail the derivation of the semi-discrete advection–diffusion problem as applied to wave-like solutions, from which the relevant eigencurves can be obtained. The inviscid case (linear advection) is then addressed in Sec. 2.2, where the role of primary and secondary eigencurves is discussed from the perspective introduced in [9]. The viscous case is subsequently considered in Sec. 2.3, where eigencurves are shown to feature irregular oscillations for problems strongly dominated by either convection or diffusion.

2.1. Spatial discretization and wave-like solutions

The linear advection–diffusion equation is given by

$$\frac{\partial u}{\partial t} + a \frac{\partial u}{\partial x} = \mu \frac{\partial^2 u}{\partial x^2}, \quad (1)$$

for $x \in \Omega \subset \mathbb{R}$ and $t \geq 0$, where a is the advection speed and μ is the viscosity. We consider periodic boundary conditions and denote by $\partial\Omega_L$ and $\partial\Omega_R$ the left and right boundaries of the domain, respectively. Following the spectral/hp discretization, we divide Ω into non-overlapping elements Ω_e such that $\Omega = \bigcup_e \Omega_e$ and approximate the numerical solution by

$$u(x, t) \approx u^\delta(x, t) = \sum_j g_j(t) \Phi_j(x), \tag{2}$$

where Φ_j are global basis functions and g_j are their respective weights or coefficients.

In modal CG formulations, the set of global basis functions is usually composed by interface and (element-wise) bubble functions. An interface function is non-zero only at the elements shared by the interface to which the function is associated. The function has a unit value at this interface and decays linearly becoming zero at the two nearest neighbouring interfaces. A bubble function, on the other hand, is of higher order (i.e. not linear) and non-zero only at the element to which it is associated. Bubble functions must become zero at interfaces. By employing these two types of basis functions, one can span a polynomial space of degree P over Ω . The case $P = 1$ implies only (linear) interface functions, while for $P > 1$ a high-order representation can be achieved. In any case, C^0 continuity of the numerical solution is guaranteed by construction. We remark that due to the periodicity condition here considered, the interface functions related to the first ($\partial\Omega_L$) and last ($\partial\Omega_R$) interfaces are one and the same, being non-zero only at the first and last mesh elements.

The problem in Eq. (1) is then required to vanish within the global approximation space, i.e.

$$\int_{\Omega} \left(\frac{\partial u^\delta}{\partial t} + a \frac{\partial u^\delta}{\partial x} - \mu \frac{\partial^2 u^\delta}{\partial x^2} \right) \Phi_i dx = 0, \text{ for } i \in \mathbb{S}_P, \tag{3}$$

where \mathbb{S}_P is the set of values of i associated with an hp approximation space of degree P . Now, since

$$\int_{\Omega} \frac{\partial^2 u}{\partial x^2} \Phi_i dx = - \int_{\Omega} \frac{\partial u}{\partial x} \frac{\partial \Phi_i}{\partial x} dx + \int_{\Omega} \frac{\partial}{\partial x} \left(\frac{\partial u}{\partial x} \Phi_i \right) dx = - \int_{\Omega} \frac{\partial u}{\partial x} \frac{\partial \Phi_i}{\partial x} dx + \left[\frac{\partial u}{\partial x} \Phi_i \right]_{\partial\Omega_L}^{\partial\Omega_R}, \tag{4}$$

where the last term on the right-hand side vanishes if periodicity is assumed, one can rewrite Eq. (3) as

$$\int_{\Omega} \frac{\partial u^\delta}{\partial t} \Phi_i dx + a \int_{\Omega} \frac{\partial u^\delta}{\partial x} \Phi_i dx + \mu \int_{\Omega} \frac{\partial u^\delta}{\partial x} \frac{\partial \Phi_i}{\partial x} dx = 0. \tag{5}$$

It is useful to express all the global basis functions Φ_j in terms of local boundary and interior (bubble) functions and to cast the above equation in terms of element-wise integrals. Global C^0 continuity will then have to be enforced through an assembly procedure, but until then the solution can be expressed locally at element Ω_e as

$$u^\delta(x, t)|_{\Omega_e} = \sum_{j=0}^P \ell_j(t) \phi_j(x), \tag{6}$$

where ϕ_j are element-wise basis functions and ℓ_j are their coefficients. More specifically, while the set $\{\phi_1, \dots, \phi_{P-1}\}$ contains the bubble functions necessary to span the polynomial space of degree P , ϕ_0 and ϕ_P are the linear functions corresponding respectively to the descending and ascending parts of the interface functions (of the global approach) associated to the boundaries of Ω_e . This sorting of the basis functions leads to a simpler correspondence between the coefficients ℓ_j and g_j . The superscript δ used in Eq. (6) will be omitted hereafter to simplify the notation.

Given that for each set of local basis functions one has $\phi_j = \partial\phi_j/\partial x = 0$ for $x \notin \Omega_e$, the elemental contribution of Eq. (5) becomes

$$\int_{\Omega_e} \frac{\partial u}{\partial t} \phi_i dx + a \int_{\Omega_e} \frac{\partial u}{\partial x} \phi_i dx + \mu \int_{\Omega_e} \frac{\partial u}{\partial x} \frac{\partial \phi_i}{\partial x} dx = 0, \tag{7}$$

which will be subsequently re-assembled into a C^0 continuous expansion. We remark that periodicity at $\partial\Omega_L$ and $\partial\Omega_R$ is implicitly assumed here. Integrating in the standard domain $\Omega_{st} = [-1, 1]$ and inserting Eq. (6) gives

$$\frac{h}{2} \int_{\Omega_{st}} \phi_i \Sigma_j \left(\frac{\partial \ell_j}{\partial t} \phi_j \right) d\xi + a \int_{\Omega_{st}} \phi_i \Sigma_j \left(\ell_j \frac{\partial \phi_j}{\partial \xi} \right) d\xi = -\mu \frac{2}{h} \int_{\Omega_{st}} \frac{\partial \phi_i}{\partial \xi} \Sigma_j \left(\ell_j \frac{\partial \phi_j}{\partial \xi} \right) d\xi, \tag{8}$$

or

$$\frac{h}{2} \sum_{j=0}^P \frac{\partial \ell_j}{\partial t} \mathbf{M}[i, j] + a \sum_{j=0}^P \ell_j \mathbf{A}[i, j] = -\mu \frac{2}{h} \sum_{j=0}^P \ell_j \mathbf{D}[i, j], \tag{9}$$

where h is the element size (assumed constant throughout the mesh) and

$$\mathbf{M}[i, j] = \int_{\Omega_{st}} \phi_i \phi_j d\xi, \quad \mathbf{A}[i, j] = \int_{\Omega_{st}} \phi_i \phi'_j d\xi, \quad \mathbf{D}[i, j] = \int_{\Omega_{st}} \phi'_i \phi'_j d\xi, \tag{10}$$

in which $\phi'_j = \partial\phi_j/\partial\xi$. In vector form, Eq. (9) reads (assuming $a \neq 0$)

$$\frac{h}{2a} \mathbf{M} \frac{\partial \vec{\ell}_e}{\partial t} + \mathbf{A} \vec{\ell}_e = -\frac{2\mu}{ah} \mathbf{D} \vec{\ell}_e, \tag{11}$$

where $\vec{\ell}_e = \{\ell_0, \dots, \ell_P\}^T$ is the vector of local coefficients of element Ω_e , while \mathbf{M} is the mass matrix and \mathbf{A} and \mathbf{D} are matrices representing the advection and diffusion terms, respectively.

Finally, the assembly procedure must be performed to introduce inter-element communication and enforce C^0 continuity. Let \mathcal{A} be the assembly matrix such that $\vec{\ell}_\Omega = \mathcal{A} \vec{g}_\Omega$, see [7] for details. Here, $\vec{g}_\Omega = \{\dots, g_j, \dots\}^T$ for $j \in \mathbb{S}_P$ while $\vec{\ell}_\Omega = \{\dots, \vec{\ell}_e, \dots\}^T$ for $\Omega_e \subset \Omega$. This way, the global counterpart of Eq. (11) can be written as

$$\frac{h}{2a} \mathbf{M}_g \frac{\partial \vec{g}_\Omega}{\partial t} = \mathbf{X}_g \vec{g}_\Omega, \quad \mathbf{X}_g = -\left(\mathbf{A}_g + \frac{2}{\text{Pe}} \mathbf{D}_g \right), \tag{12}$$

where $\text{Pe} = ah/\mu$ is the Péclet number and the global matrices \mathbf{M}_g , \mathbf{A}_g and \mathbf{D}_g are defined by

$$\mathbf{M}_g = \mathcal{A}^T \mathbf{M}_\Omega \mathcal{A}, \quad \mathbf{A}_g = \mathcal{A}^T \mathbf{A}_\Omega \mathcal{A}, \quad \mathbf{D}_g = \mathcal{A}^T \mathbf{D}_\Omega \mathcal{A}, \tag{13}$$

according to the block-diagonal structure illustrated in Fig. 1, see [7] for details.

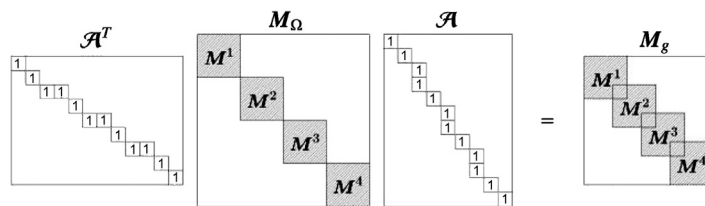


Fig. 1. Example of the global matrices obtained through the assembly procedure for the case $P = 2$ and four elements. Adapted from [7].

As pointed out in [6], a pattern can be recognized in these global matrices which allows for the decoupling of individual elements (along with their immediate neighbours) from the global system of equations. This pattern is shown in Fig. 2, where we highlight the relevant matrices for the central element and its left and right neighbours. We stress that due to the assembly structure of the periodic problem considered, the matrices highlighted in Fig. 2 are the same for all the elements. Moreover, we note that these matrices have size $P \times P$ because the last coefficient of a given element is now only considered (as the first one) in the expansion of the following mesh element. As a result, the relevant central (\mathcal{C}), left (\mathcal{L}) and right (\mathcal{R}) matrices of Fig. 2 are defined directly from the block matrices (generically referred to as \mathcal{B}) respectively composing the global matrices \mathbf{M}_g , \mathbf{A}_g and \mathbf{D}_g defined in Eq. (13), so that

$$\mathcal{C} = \mathcal{B}[1 : P, 1 : P], \tag{14}$$

$$\mathcal{L}[1, 1 : P] = \mathcal{B}[P + 1, 1 : P], \quad \mathcal{L}[2 : P, 1 : P] = \mathcal{O}, \tag{15}$$

$$\mathcal{R}[1 : P, 1] = \mathcal{B}[1 : P, P + 1], \quad \mathcal{R}[1 : P, 2 : P] = \mathcal{O}, \tag{16}$$

where \mathcal{O} denotes null matrices of the required size. Note that we use the notation $p : q$ above to refer to the complete set of integers ranging from p to q .

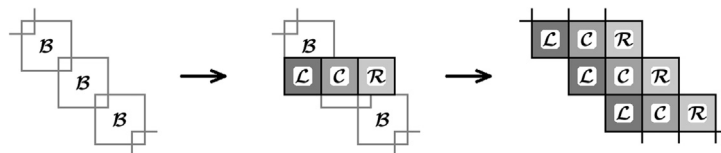


Fig. 2. Structure of the global matrices, highlighting the relevant central (\mathcal{C}), left (\mathcal{L}) and right (\mathcal{R}) matrices defined directly from the block matrices (\mathcal{B}) which form a given global matrix.

The resulting decoupled semi-discrete advection–diffusion problem is given in vector form by

$$\frac{h}{2a} \left(\mathcal{L}_M \frac{\partial \vec{c}_L}{\partial t} + \mathcal{C}_M \frac{\partial \vec{c}}{\partial t} + \mathcal{R}_M \frac{\partial \vec{c}_R}{\partial t} \right) = \mathcal{L}_X \vec{c}_L + \mathcal{C}_X \vec{c} + \mathcal{R}_X \vec{c}_R, \tag{17}$$

where the subscripts \mathbf{M} and \mathbf{X} indicate the block matrices (\mathcal{B}) from which \mathcal{C} , \mathcal{L} and \mathcal{R} were obtained. In addition, $\vec{c} = \{\ell_0, \dots, \ell_{P-1}\}^T$ is the reduced vector of coefficients associated to the central element, while \vec{c}_L and \vec{c}_R correspond to the reduced vectors of the neighbouring elements from the left and right sides, respectively. We stress that Eq. (17) stems directly from Eq. (12) without any assumptions, just like individual equations in a system hold independently. Periodicity is used when we assume that Eq. (17) can be applied for all the mesh elements, which is readily justified since the global coupling can then be regarded as cyclic.

For the eigensolution analysis, one seeks for solutions in the form (hereafter, $i = \sqrt{-1}$)

$$u = \exp[i(kx - wt)], \tag{18}$$

or, more specifically, solutions in which the element-wise approximating coefficients are related to the above wave-like solution through projection. A local or element by element projection of Eq. (18) leads to

$$\mathbf{M}_\Omega \vec{\ell}_\Omega = \vec{I}_\Omega, \tag{19}$$

where $\vec{I}_\Omega = \{\dots, \vec{I}_e, \dots\}^T$ and $\vec{I}_e = \int_{\Omega_{st}} \{u_e \phi_0, \dots, u_e \phi_P\}^T d\xi$, in which $u_e = u(x_e + \xi h/2, t)$ with $\xi \in \Omega_{st}$, x_e being the mid-point of Ω_e . Performing the assembly procedure and the subsequent decoupling of individual elements (with their immediate neighbours) yields

$$\mathcal{A}^T \mathbf{M}_\Omega \mathcal{A} \vec{g}_\Omega = \mathcal{A}^T \vec{I}_\Omega \Rightarrow \mathbf{M}_g \vec{g}_\Omega = \mathcal{A}^T \vec{I}_\Omega \Rightarrow \mathcal{L}_M \vec{c}_{e-1} + \mathcal{C}_M \vec{c}_e + \mathcal{R}_M \vec{c}_{e+1} = \vec{I}_e, \tag{20}$$

where

$$\vec{I}_e = \int_{\Omega_{st}} \{u_{e-1} \phi_P + u_e \phi_0, u_e \phi_1, \dots, u_e \phi_{P-1}\}^T d\xi = \vec{\zeta} \exp[i(kx_e - wt)], \tag{21}$$

in which $\vec{\zeta} = \{\exp(-ikh) \pi_P + \pi_0, \pi_1, \dots, \pi_{P-1}\}^T$ and $\pi_j(kh) = \int_{\Omega_{st}} \exp(ikh\xi/2) \phi_j(\xi) d\xi$.

In order to extract \vec{c}_e from Eq. (20) we note that, owing to the solution periodicity and equispaced mesh employed, $\vec{c}_{e\pm 1} \langle u(x) \rangle = \vec{c}_e \langle u(x \pm h) \rangle$, where $\langle \cdot \rangle$ is used to denote a functional dependence on $u(x)$. In addition, since $\vec{I}_e \langle u(x \pm h) \rangle = \exp(\pm ikh) \vec{I}_e \langle u(x) \rangle$ from Eq. (21), one has therefore $\vec{c}_{e\pm 1} = \exp(\pm ikh) \vec{c}_e$ and thus

$$\vec{c}_e = \left[\mathcal{L}_M e^{-ikh} + \mathcal{C}_M + \mathcal{R}_M e^{+ikh} \right]^{-1} \vec{I}_e. \tag{22}$$

In the temporal eigensolution's approach, one should use Eqs. (22) and (21) with real k and complex w into the semi-discrete advection problem in Eq. (17) to obtain

$$\frac{h}{2a} (-iw) \left[\mathcal{L}_M e^{-ikh} + \mathcal{C}_M + \mathcal{R}_M e^{+ikh} \right] \vec{c} = \left[\mathcal{L}_X e^{-ikh} + \mathcal{C}_X + \mathcal{R}_X e^{+ikh} \right] \vec{c}, \tag{23}$$

which, by defining

$$\mathcal{Z} = 2 \left[\mathcal{L}_M e^{-ikh} + \mathcal{C}_M + \mathcal{R}_M e^{+ikh} \right]^{-1} \left[\mathcal{L}_X e^{-ikh} + \mathcal{C}_X + \mathcal{R}_X e^{+ikh} \right], \tag{24}$$

is equivalent to

$$-i \frac{wh}{a} \vec{\zeta} = \mathcal{Z} \vec{\zeta}. \tag{25}$$

In general, one is left with an eigenvalue problem with P solutions owing to the size of \mathcal{Z} . The resulting eigenvalue/eigenvector pairs (λ_m, \vec{v}_m) are related to the problem variables by

$$w_m = \frac{ia}{h} \lambda_m \text{ and } \vec{\zeta}_m \propto \vec{v}_m, \tag{26}$$

in which, without loss of generality, we define $\vec{\zeta}_m = \vec{v}_m/s_m$, where s_m is the sum of the entries of \vec{v}_m . The general numerical solution can readily be obtained from Eq. (22) since, through the right-hand side of Eq. (21), one has

$$\vec{I}_e(t) = \sum_{m=0}^{P-1} Z_m \vec{v}_m \exp[i(kx_e - w_m t)], \tag{27}$$

where the scalar coefficients Z_m are obtained from the initial condition. For instance, if $u = \exp(ikx)$ at the initial state, Eqs. (21) and (27) written at $t = 0$ yield

$$\sum_{m=0}^{P-1} Z_m \bar{v}_m \exp(ikx_e) = \bar{\zeta} \exp(ikx_e). \tag{28}$$

Accordingly, $\bar{Z} = \{Z_0, \dots, Z_{P-1}\}^T$ is given by

$$\bar{Z} = \mathcal{V}^{-1} \bar{\zeta}, \tag{29}$$

where $\mathcal{V} = \{\bar{v}_0, \dots, \bar{v}_{P-1}\}$. We note that $\bar{\zeta}$ represents the elemental Galerkin projection of the Fourier modes $\exp(ikx)$ onto the polynomial basis which is then projected through matrix \mathcal{V}^{-1} onto the discrete eigenbasis of the PDE being discretized.

2.2. The inviscid case ($\mu = 0$)

Before discussing advection–diffusion in general, it is useful to analyse how CG behaves for pure advection. As it is customary in wave propagation analysis, the relation $w = ak$ will be used to define a modified wavenumber k^* for each numerical angular frequency w_m , such that $w_m = ak_m^*$. The natural interpretation is that each mode (m) of the numerical solution will behave as if related to k_m^* instead of k . We note from Eqs. (24)–(26) that both w_m and k_m^* are functions of the ‘baseline’ wavenumber k .

The dispersion and diffusion curves for polynomial orders $P = 1$ and $P = 2$ are shown in Fig. 3. In both cases, there is no diffusion error and thus no numerical dissipation for all wavenumbers. This was verified to hold regardless of P . The dispersion curves, however, display significant numerical error for the poorly-resolved wavenumbers ($kh/P \rightarrow \pi$). For small wavenumbers though, the linear behaviour of the exact dispersion relation ($k^* = k$) is recovered as expected. This linear region is larger for $P = 2$ due to the higher order and thus superior accuracy of the discretization, but there is a secondary mode present which corresponds to the thin continuous branch in the bottom left plot of Fig. 3. The discrete bullets shown correspond to the eigencurves obtained from classical analysis, available for linear and quadratic discretizations [8] and given respectively by

$$k^*h = \frac{3 \sin(kh)}{2 + \cos(kh)} \text{ and } k^*h = \frac{-4 \sin(kh) \pm 2\sqrt{[\cos(kh) - 1][\cos(kh) - 19]}}{3 - \cos(kh)}. \tag{30}$$

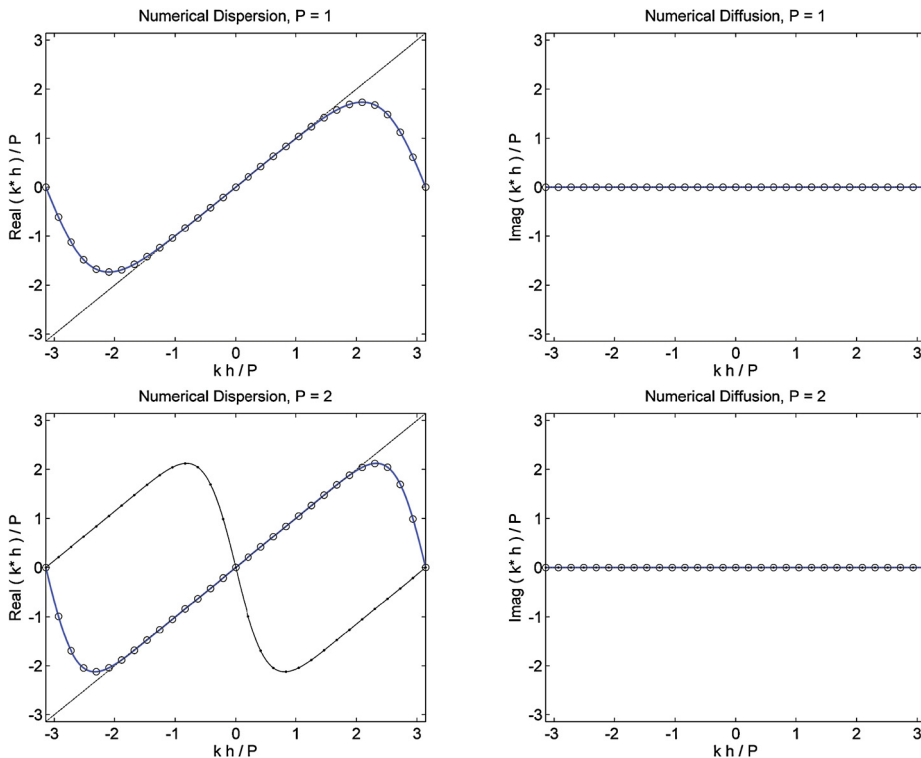


Fig. 3. Dispersion–diffusion curves for pure advection with CG for $P = 1$ (top) and $P = 2$ (bottom). The thick blue branches represent the primary eigen-curves, dashed lines indicate the exact behaviour and discrete bullets depict the analytical results from classical analyses.

The role of secondary eigencurves in the context of spectral/*hp* methods has been interpreted in different ways in the literature. However, as pointed out in [5], generally they are simply regarded as ‘spurious’ and entirely neglected. A new perspective on the matter was introduced in [9], where secondary modes are interpreted as replications of the primary mode (the one that recovers $k^* = k$ as $k \rightarrow 0$). While that work focused on the discontinuous Galerkin (DG) formulation, the present work extends this interpretation to the CG method. As in [9], here the eigencurves were also verified to be equispaced in the (periodic) normalized \bar{k} axis, where here $\bar{k} = kh/P$ rather than $kh/(P + 1)$, which was the case for DG. As a result, the modified wavenumber for each mode can be obtained from the relation

$$\overline{k_m^*}(\bar{k}) = \overline{k_0^*}(\bar{k} + 2\pi m/P), \quad m = 0, \dots, P - 1, \tag{31}$$

in which the zeroth mode was taken (without loss of generality) as the primary one. We remark that $\overline{k_0^*}$ is periodic as a function of \bar{k} , with period 2π , and that the above relation holds for both real and imaginary parts of $\overline{k_m^*}$.

Now, upon increasing P , the imaginary part of all the eigencurves was found to remain identically zero, indicating the absence of numerical dissipation for the CG discretization of the linear advection equation, which is consistent with classical low-order CG analysis [8]. An unexpected behaviour was however observed for the dispersion eigencurves for the higher-order discretizations. These are depicted in Fig. 4 for polynomial orders varying from 3 to 6. The left column shows all the (dispersion) eigencurves while the right column shows only the primary ones, along with the exact dispersion relation $k^* = k$. The primary eigencurves for each P are also highlighted in the plots of the left column for reference. An unusual feature of these curves is their discontinuous character, which is very mild when $P = 3$, but is already quite significant for $P = 6$. Such discontinuities cannot be avoided since they originate from the separated (upper/lower) branches shown in the ‘all-eigencurves’ plots of Fig. 4. We note that a similar behaviour, i.e. separated branches leading to discontinuities, has been observed both for DG and SV (spectral volume) methods when central fluxes are used instead of upwind ones, see e.g. Ref. [3].

Note that we defined the primary eigencurve as the one that recovers $k^* = k$ as $k \rightarrow 0$. Away from $k = 0$, however, the identification of the primary curve is less obvious since eigencurves can cross each other and even appear as separated branches, making the definition of the primary eigencurve somewhat arbitrary. Still, the trends observed for the lower-order discretizations (where there is less ambiguity) point out a way to define the primary curve as the polynomial order increases. More specifically, a linear region around $k = 0$ and a crossing of the horizontal axis with negative slope at $\bar{k} = \pm\pi$ are expected. When these features are taken into account, it is only natural (see Fig. 4) to consider the ‘arches’ of separated branches as parts of the primary eigencurve. The resulting curve is then readily verified to obey the replication property (Eq. (31)) since all the remaining eigencurves can be recognized as replicas of the primary one. There remains to define precisely the extent of each arch, i.e. the position of the discontinuous jumps of the primary eigencurve. In our study, these positions have been defined so as to minimize the magnitude of the jumps, the minimization being performed over the relevant range of wavenumbers where distinct branches are closest. But this last definition is arbitrary and the replication property could still hold with a different specification for the jumps location.

A larger number of discontinuities per curve was observed for $P > 6$ (not shown) as more branches on the central section of all-eigencurves plots begin to detach as P increases, generating additional separated (upper/lower) branches. This non-smooth character on dispersion eigencurves might introduce potentially undesirable dispersive features on the numerical solution. It should be noted nevertheless that the linear (central) region of the primary eigencurves approximates the exact dispersion behaviour quite accurately. Still, we point out that high-order CG spectral/*hp* discretizations may feature irregular dispersive behaviour for under-resolved simulations of pure advection, where the wavenumbers involved might lie outside the linear region of the eigencurves. This should be specially true for higher-order discretizations where the number and intensity of discontinuities is larger, as discussed above.

Regarding the fact that secondary eigencurves can be understood as replicas of a primary curve, recall Eq. (31), it is clear that all the information concerning numerical dispersion and diffusion characteristics can be obtained directly from the primary eigencurve. This not only simplifies subsequent analysis, but also justifies why secondary curves can be cast aside for most purposes. However, as demonstrated in [9], secondary modes should not be considered spurious since some of them can contribute to the overall accuracy of the numerical solution. The argument used in [9] for such demonstration can be easily adapted for the CG case and is described in the following.

Since Fourier and piecewise polynomial approximation spaces are fundamentally different, a single Fourier component given to the numerical scheme through a Galerkin projection will energize several (P) numerical polynomial modes. However, these polynomial modes are perceived by the numerical setting as if related to different ‘apparent’ wavenumbers $(\bar{k} + 2\pi m/P)$ as made explicit in Eq. (31). The CG scheme will then propagate them, as the primary eigencurve prescribes, in accordance with each of their apparent wavenumbers. As a result, those modes whose apparent wavenumbers lie within the (approximately) linear region of the primary eigencurve will be propagated without significant dispersion or diffusion errors. These modes will therefore contribute to preserve the solution at the initial state, which, coming from a Galerkin projection, constitute the best approximation (in the L^2 sense) to the Fourier component considered initially. The remaining eigenmodes, i.e. those whose apparent wavenumbers lie outside the linear region of the primary eigencurve, will introduce dispersion and diffusion errors and thus can be regarded as unphysical. Fortunately, such unphysical modes are expected to have negligible energy if the original Fourier component is reasonably resolved by the *hp* setting employed. The interested reader is referred to reference [9] for a more detailed discussion.

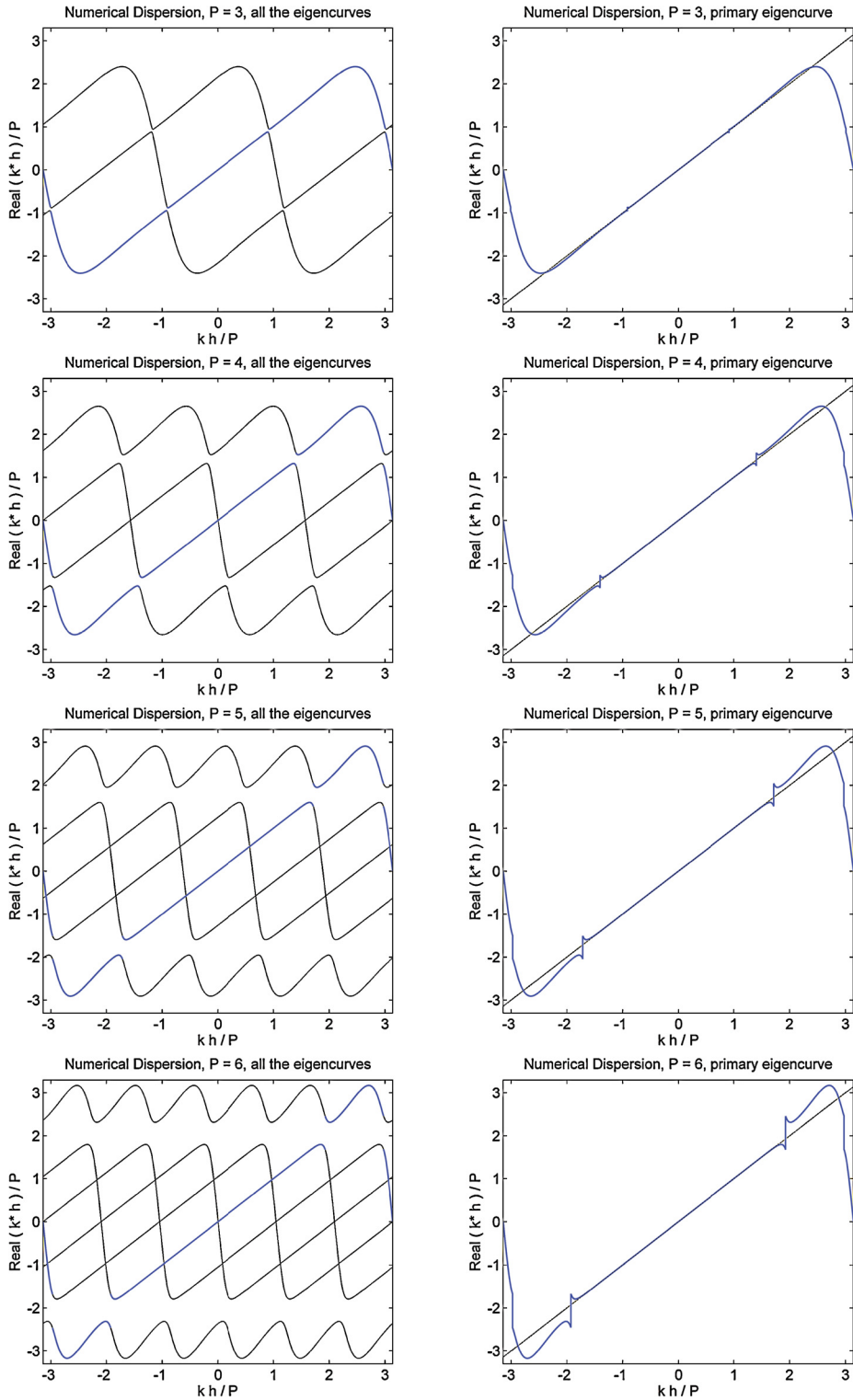


Fig. 4. Dispersion curves for pure advection with CG for $P = 3, \dots, 6$ (top to bottom). The plots on the left show all the eigencurves and those on the right show only the primary curves and the exact behaviour (dashed line). Primary curves are also highlighted (in blue colour) on the left-hand side plots.

2.3. The viscous case ($\mu > 0$)

The exact behaviour for the advection–diffusion problem can be derived by introducing Eq. (18) into Eq. (1), which yields $w = ak - i\mu k^2$. Since $k^* = w/a$, one has

$$\frac{k^*h}{P} = \frac{kh}{P} - i \frac{\mu P}{ah} \left(\frac{kh}{P}\right)^2 \Leftrightarrow k^*\bar{h} = k\bar{h} - i \frac{(k\bar{h})^2}{Pe^*}, \tag{32}$$

where $Pe^* = a\bar{h}/\mu$ and $\bar{h} = h/P$. The relation on the right-hand side of Eq. (32) makes clear that the normalized dispersion–diffusion curves of the advection–diffusion problem should depend on Pe^* alone, which already takes into account the discretization order P employed (in terms of scaling).

The eigencurves obtained for the CG discretization of the advection–diffusion problem with $Pe^* = 10$ are given in Fig. 5 for $P = 1$ and $P = 2$. The dispersion curves are similar to those obtained for the inviscid case (see Fig. 3) while the diffusion curves are obviously different. The discrete bullets shown correspond to the eigencurves obtained from classical analysis, available for linear and quadratic discretizations [8] and given respectively by

$$k^*h = \frac{3 \sin(kh) + 6i[\cos(kh) - 1]/Pe^*}{2 + \cos(kh)} \quad \text{and} \quad k^*h = \frac{-4 \sin(kh) - 2i[2 \cos(kh) + 13]/Pe^* \pm 2\sqrt{\Delta}}{3 - \cos(kh)}, \tag{33}$$

where

$$\Delta = [\cos(kh) - 1][\cos(kh) - 19] - i \sin(kh)[7 \cos(kh) - 97]/Pe^* + [11 \cos^2(kh) - 112 \cos(kh) - 124]/(Pe^*)^2. \tag{34}$$

The exact behaviour obtained from Eq. (32) is depicted through the dashed curves shown in Fig. 5. The primary eigenmodes accurately follow the correct behaviour for a reasonable range of wavenumbers. Regarding diffusion in particular, extra dissipation is introduced as numerical error for the poorly-resolved (highest) wavenumbers. This numerical diffusion becomes more significant for higher-order discretizations, as discussed below.

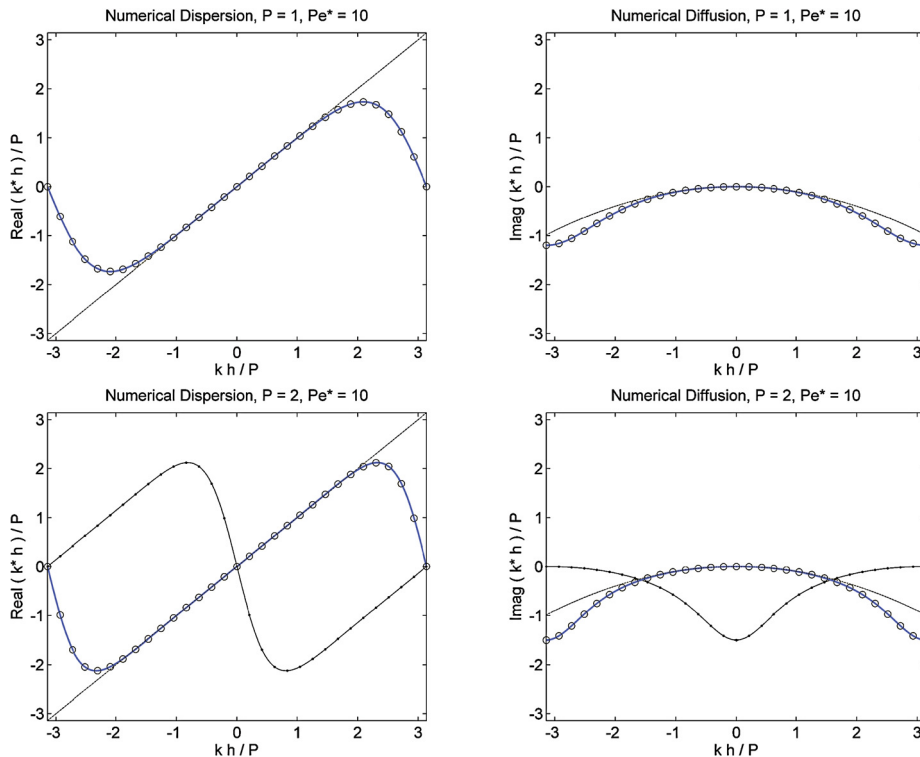


Fig. 5. Dispersion–diffusion eigencurves for $P = 1$ (top) and $P = 2$ (bottom) for the advection–diffusion problem with $Pe^* = 10$. The thick blue branches represent the primary eigencurves, dashed curves indicate the exact behaviour and discrete bullets depict classical analytical results.

Cases $P = 3, \dots, 6$, again for $Pe^* = 10$, are shown in Fig. 6. The range of wavenumbers for which the (primary) eigen-curves reproduce well the exact relation given by Eq. (32) becomes larger with increasing P . For the poorly-resolved wavenumbers, the amount of numerical error introduced also increases with the polynomial order both for dispersion and diffusion. These features are likewise observed for the DG formulation [9]. We note that the discontinuities seen on the eigencurves of pure advection (Fig. 4) for higher values of P are somehow inhibited here by the viscous effects.

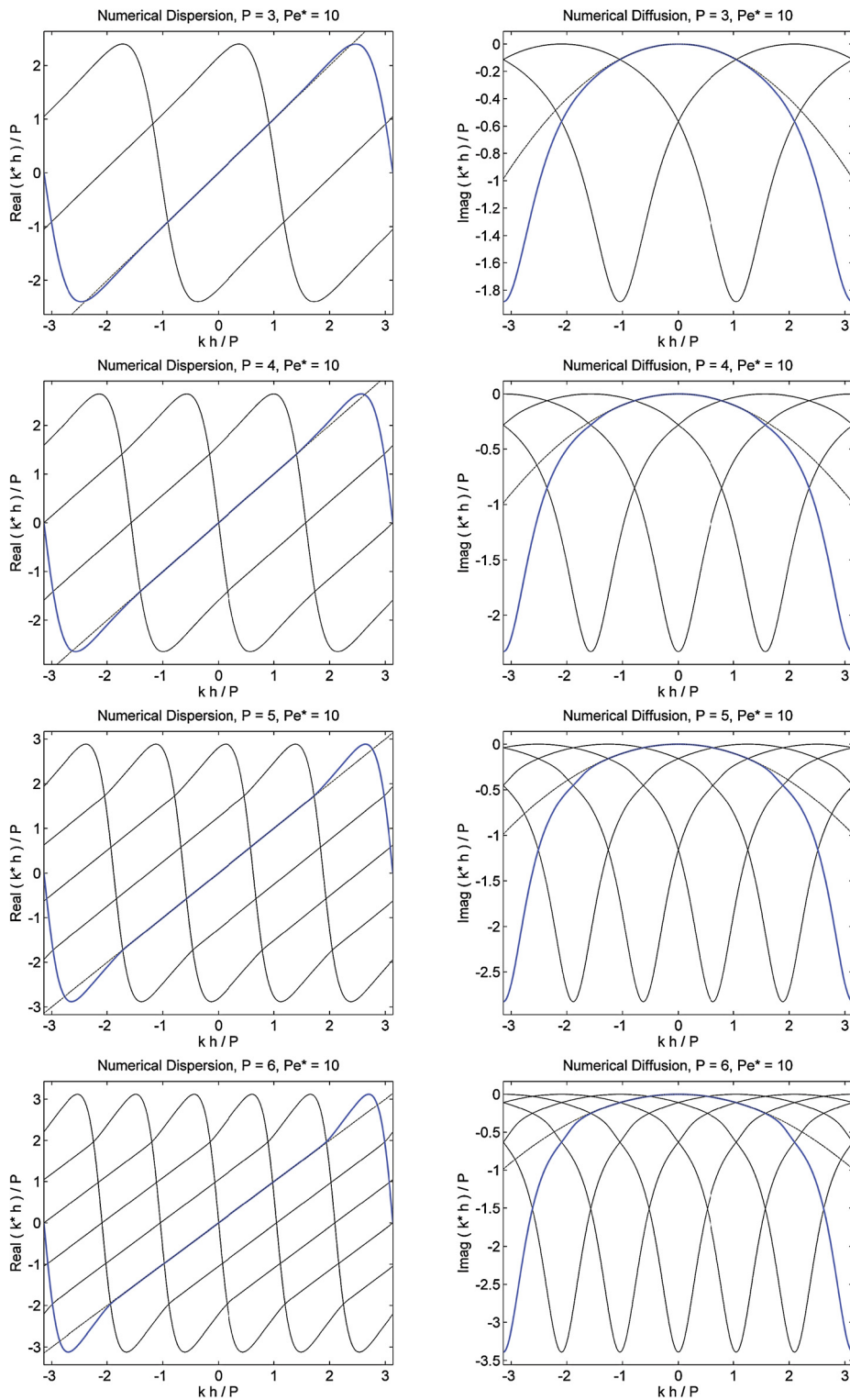


Fig. 6. Dispersion–diffusion eigencurves for $P = 3, \dots, 6$ (top to bottom) for the advection–diffusion problem with $Pe^* = 10$. The thick highlighted branches (in blue colour) represent primary eigencurves while dashed curves indicate the exact behaviour.

Nevertheless, for $Pe^* \rightarrow \infty$ ($\mu \rightarrow 0$), not only discontinuities begin to appear on the dispersion curves, but also unusual features become apparent on diffusion curves. This is illustrated in the plots on the upper half of Fig. 7, where case $P = 3$ is considered with $Pe^* = 10^2$ and $Pe^* = 10^3$. In addition, non-smooth behaviours are also observed when $Pe^* \rightarrow 0$, i.e. for

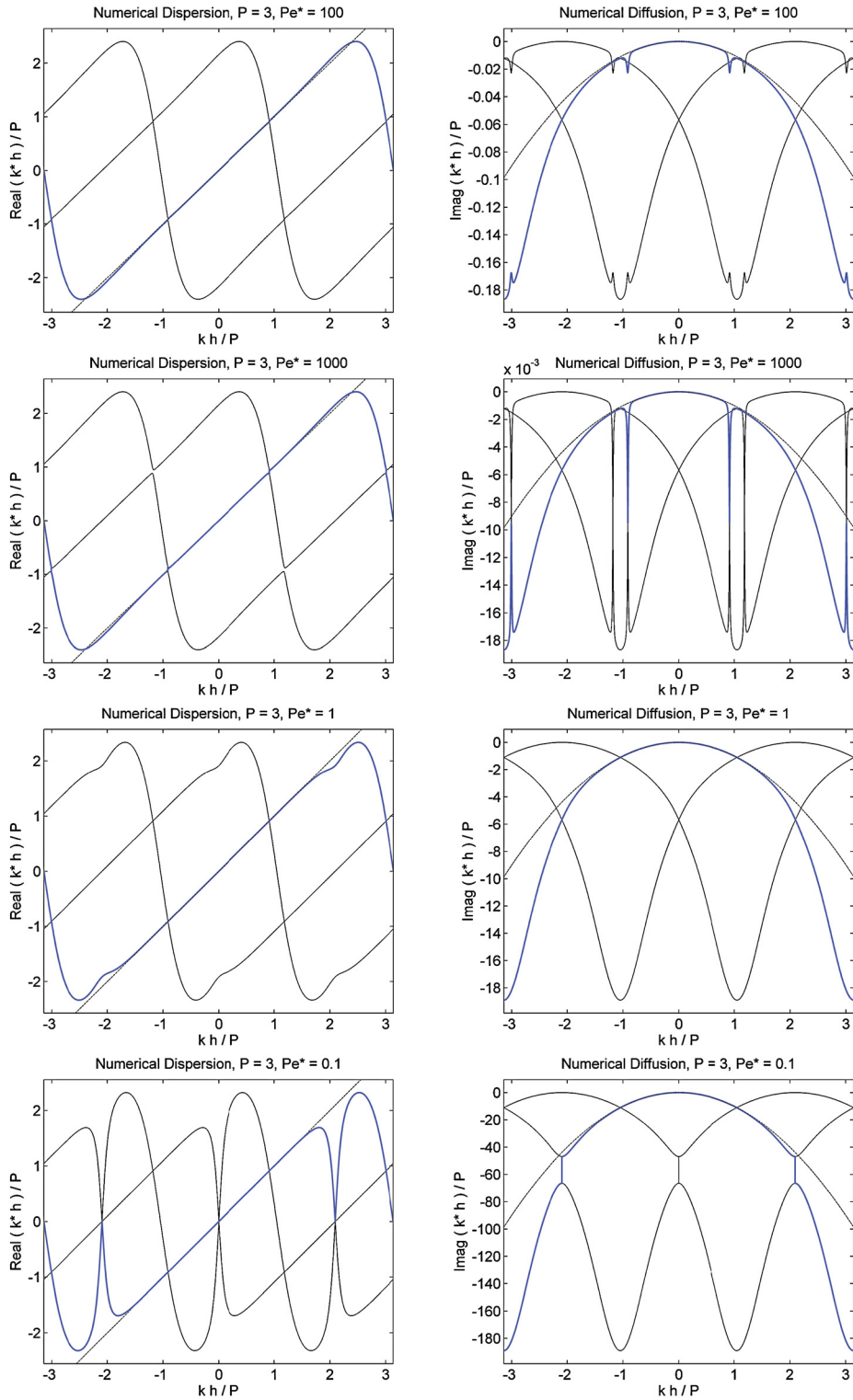


Fig. 7. Dispersion–diffusion eigencurves for $P = 3$ for the advection–diffusion problem with $Pe^* = 10^2$, $Pe^* = 10^3$, $Pe^* = 1$ and $Pe^* = 10^{-1}$ (top to bottom). The thick highlighted branches (in blue colour) represent primary eigencurves while dashed curves indicate the exact behaviour.

diffusion-dominated problems, as shown in the plots on the lower half of Fig. 7, where case $P = 3$ is considered with $Pe^* = 1$ and $Pe^* = 10^{-1}$. Such results raise a question on the suitability of high-order spectral/hp CG formulations for under-resolved simulations of problems dominated by either advection or diffusion. We acknowledge that within the context of high-order

methods, the unsuitability for under-resolved simulations is not new (schemes becoming unstable at higher orders). We also note that, due to truncation errors, there is no practical scheme free from dispersion/diffusion errors at the marginally resolved scales. Still, it is important to bear in mind the nature and extent of such errors in order to apply the chosen numerical method in a sensible manner, regarding both accuracy and stability.

3. Stabilized advection with CG

This section is devoted to the dispersion–diffusion analysis of the spectral/*hp* CG formulation with added spectral vanishing viscosity (SVV). The linear advection equation with SVV-based stabilization is discussed in Sec. 3.1, where the implementation of the standard SVV operator is also described in detail. Sec. 3.2 addresses potential issues of the traditional SVV operator due to its dependency on a variable Péclet number. Sec. 3.3 discusses how the Péclet number can be made globally constant and thus introduces a more reliable SVV approach. A new SVV kernel function is also proposed in Sec. 3.3 which provides a consistent increase in the range of wavenumbers not affected by the SVV as the polynomial order is increased.

3.1. Spectral vanishing viscosity

Since the standard CG formulation provides no numerical dissipation for pure advection problems, the basic purpose of a spectral vanishing viscosity (SVV) operator is to introduce a limited amount of diffusion at higher wavenumbers in order to further stabilize the CG scheme and increase its robustness for the solution of non-linear problems dominated by advection.

The advection equation augmented with SVV reads

$$\frac{\partial u}{\partial t} + a \frac{\partial u}{\partial x} = \mu \frac{\partial}{\partial x} \left(\mathcal{Q} \star \frac{\partial u}{\partial x} \right), \tag{35}$$

where μ is the base SVV magnitude and $\mathcal{Q} \star (\cdot)$ represents the (normalized) SVV operator acting on the solution derivatives. The SVV technique was first introduced for pure spectral methods [10] and its use in Fourier space can easily be implemented as a multiplication between the Fourier coefficients of the solution (\hat{u}_k) and those of the SVV kernel (\hat{Q}_k), so that

$$\mu \frac{\partial}{\partial x} \left(\mathcal{Q} \star \frac{\partial u}{\partial x} \right) = -\mu \sum_k k^2 \hat{Q}_k \hat{u}_k \exp(ikx). \tag{36}$$

The idea is to activate the SVV dissipation only at the highest wavenumbers. Originally, kernel entries were defined as $\hat{Q}_k = 1$ for $k > m$ and zero otherwise [10], m being the wavenumber threshold above which dissipation is introduced. Subsequently, as it was recognized that discontinuous kernel variations could be detrimental to the formulation, smooth definitions were proposed, such as $\hat{Q}_k = \exp[-(k - n)^2 / (k - m)^2]$ for $k > m$ and zero otherwise [20], n being the total number of modes employed.

The discretization of Eq. (35) given below will follow closely that discussed in Sec. 2.1. Beginning from Eq. (35) and performing essentially the same initial steps yields

$$\int_{\Omega_e} \frac{\partial u}{\partial t} \phi_i dx + a \int_{\Omega_e} \frac{\partial u}{\partial x} \phi_i dx + \mu \int_{\Omega_e} \left(\mathcal{Q} \star \frac{\partial u}{\partial x} \right) \frac{\partial \phi_i}{\partial x} dx = 0, \tag{37}$$

which should be compared with Eq. (7). Casting integrations into Ω_{st} gives

$$\frac{h}{2} \int_{\Omega_{st}} \phi_i \Sigma_j \left(\frac{\partial \ell_j}{\partial t} \phi_j \right) d\xi + a \int_{\Omega_{st}} \phi_i \Sigma_j \left(\ell_j \frac{\partial \phi_j}{\partial \xi} \right) d\xi = -\mu \frac{2}{h} \int_{\Omega_{st}} \frac{\partial \phi_i}{\partial \xi} \mathcal{Q} \star \left[\Sigma_j \left(\ell_j \frac{\partial \phi_j}{\partial \xi} \right) \right] d\xi. \tag{38}$$

The multiplication between \hat{Q}_k and \hat{u}_k used in Fourier space, Eq. (36), is here accommodated as a multiplication between kernel entries and element-wise modal coefficients. Note that these are not ℓ_j , but instead the coefficients of $\Sigma_i \ell_i \phi'_i$, which will be called ℓ'_j and evaluated through projection, i.e.

$$\int_{\Omega_{st}} \left(\Sigma_i \ell_i \phi'_i - \Sigma_j \ell'_j \phi_j \right) \phi_k d\xi = 0 \Rightarrow \sum_{i=0}^P \ell_i \int_{\Omega_{st}} \phi'_i \phi_k d\xi = \sum_{j=0}^P \ell'_j \int_{\Omega_{st}} \phi_j \phi_k d\xi \Rightarrow \mathbf{A} \vec{\ell} = \mathbf{M} \vec{\ell}', \tag{39}$$

so that $\vec{\ell}' = \mathbf{M}^{-1} \mathbf{A} \vec{\ell}$, see Eq. (10) for the definition of these matrices. As a result, one would have

$$\mathcal{Q} \star \left(\Sigma_j \ell_j \phi'_j \right) = \mathcal{Q} \star \left(\Sigma_j \ell'_j \phi_j \right) = \mathcal{Q} \star \left(\vec{\phi}^T \vec{\ell}' \right) = \vec{\phi}^T \mathcal{Q} \vec{\ell}', \tag{40}$$

where \mathcal{Q} is a diagonal matrix whose entries are the kernel components \hat{Q}_k associated to the operator \mathcal{Q} . We stress that a consistent sorting must be used for the entries of $\vec{\phi}^T$ and $\vec{\ell}'$ to take into account the hierarchical nature of the basis functions employed in accordance with the kernel components.

The implementation in Eq. (40) was used in early applications of SVV to the CG formulation [13], but was soon recognized as not ideal because the CG set of (boundary/bubble) basis functions is not orthogonal. An alternative strategy was then employed in subsequent works [15,21,14] which writes the expansion $\sum_j \ell'_j \phi_j$ on a set of orthogonal basis functions, applies the SVV filtering operation (embodied in \mathcal{Q}), and then rewrites the filtered expansion on its original set of basis functions. In this improved implementation, instead of Eq. (40), one has

$$\mathcal{Q} \star \left(\sum_j \ell_j \phi'_j \right) = \mathcal{Q} \star \left(\sum_j \ell'_j \phi_j \right) = \mathcal{Q} \star \left(\vec{\phi}^T \vec{\ell}' \right) = \vec{\phi}^T \mathcal{T}^{-1} \mathcal{Q} \mathcal{T} \vec{\ell}', \tag{41}$$

where \mathcal{T} is the transformation matrix from the CG basis employed to a suitable orthogonal basis. The orthonormal set of Legendre basis functions (popular nowadays in modal DG formulations) has been typically chosen for the process, in which case

$$\mathcal{T}[i, j] = \int_{\Omega_{st}} \psi_i \phi_j d\xi, \tag{42}$$

where ψ_i , for $i = 0, \dots, P$, are the modal DG's usual Legendre orthonormal basis functions, so that $\vec{\ell}'_{DG} = \mathcal{T} \vec{\ell}'_{CG}$. Introducing Eq. (41) into Eq. (38) yields

$$\frac{h}{2} \sum_{j=0}^P \frac{\partial \ell_j}{\partial t} \mathbf{M}[i, j] + a \sum_{j=0}^P \ell_j \mathbf{A}[i, j] = -\mu \frac{2}{h} \sum_{j=0}^P \ell_j \mathbf{D}_{\mathcal{Q}}[i, j], \tag{43}$$

which is similar to Eq. (9) except for the fact that matrix \mathbf{D} is now replaced by

$$\mathbf{D}_{\mathcal{Q}} = \mathbf{A}^T \mathcal{T}^{-1} \mathcal{Q} \mathcal{T} \mathbf{M}^{-1} \mathbf{A}, \tag{44}$$

since $\mathbf{A}^T[i, j] = \int_{\Omega_{st}} \phi'_i \phi_j d\xi$ and $\vec{\ell}' = \mathbf{M}^{-1} \mathbf{A} \vec{\ell}$. In vector form, Eq. (43) reads (assuming $a \neq 0$)

$$\frac{h}{2a} \mathbf{M} \frac{\partial \vec{\ell}}{\partial t} + \mathbf{A} \vec{\ell} = -\frac{2\mu}{ah} \mathbf{D}_{\mathcal{Q}} \vec{\ell}, \tag{45}$$

which is the counterpart of Eq. (11) with $\mathbf{D}_{\mathcal{Q}}$ in place of \mathbf{D} .

The rest of the discretization process (global assembly, decoupling of reduced eigensystems, etc.) is formally identical to that conducted in Sec. 2.1, the only difference being that $\mathbf{D}_{\mathcal{Q}}$ is used instead of \mathbf{D} . Hence, the dispersion–diffusion characteristics associated to Eq. (45) are completely defined by the kernel entries \hat{Q}_k , the polynomial order P and the Péclet number $Pe = ah/\mu$, or, equivalently, by \hat{Q}_k , P and $Pe^* = Pe/P$.

3.2. Analysis of traditional SVV operators

For a given Pe^* , the regular (second-order) diffusion operator is expected to provide a parabolic-like profile for the diffusion eigencurves, recall Eq. (32). On the other hand, SVV operators are primarily designed to introduce dissipation only at the highest (poorly-resolved) wavenumbers. Hence, SVV kernel entries \hat{Q}_k become non-zero only for modes above a prescribed threshold P_{SVV} . A widely used “exponential” kernel was proposed in [20], where

$$\hat{Q}_k = \exp \left[-\frac{(k - P)^2}{(k - P_{SVV})^2} \right], \text{ for } k > P_{SVV}. \tag{46}$$

The kernel's behaviour is shown in Fig. 8 when $Pe^* = 3$ (for $P = 2$) and $Pe^* = 6$ (for $P = 4$). In both cases $P_{SVV} = 0$. The parabolic profiles associated with each Pe^* are shown as thin dashed lines on the diffusion plots of Fig. 8. Only the primary eigencurves are depicted owing to the replication property discussed in Sec. 2.2.

When employing SVV, the current practice (see e.g. [13] and references therein) is to use $\mu = \mu_0/P$, μ being the base SVV magnitude, recall Eq. (35), and μ_0 a fixed parameter. Note that doing this implicitly makes $Pe^* = ah/\mu P$ independent of P . This practice will hereafter be called the “traditional” SVV approach. We stress, however, that Pe^* still depends on the product ah which, in practical simulations, will vary since the advection speed and the mesh spacing are essentially independent of each other. To illustrate this behaviour, consider a linear advection problem (i.e. given a) to be solved by CG with SVV-based stabilization. Following the traditional approach, one has $\mu \propto P^{-1}$. Given the total number of degrees of freedom (i.e. fixed h/P), consider two discretization spaces: (i) $P_1 = 2$ and $h_1 = h$, so that $Pe_1^* = ah_1/\mu_1 P_1 = 3$; (ii) $P_2 = 4$ and $h_2 = 2h$, so that $Pe_2^* = ah_2/\mu_2 P_2 = 6$. For these cases, the behaviour of the (exponential kernel-based) SVV operator is that already shown in Fig. 8. The diffusion plots highlight the problem of the traditional approach: SVV will have essentially different effects on a given physical problem for the same range of wavenumbers (recall that h/P is fixed). In particular,

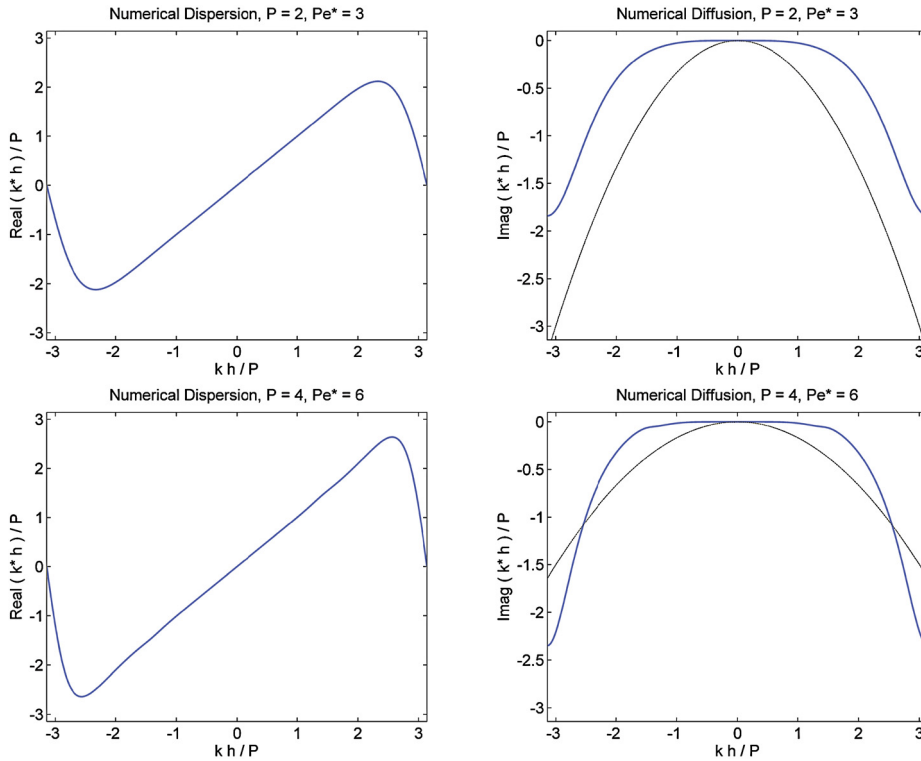


Fig. 8. Dispersion–diffusion eigencurves for the exponential SVV kernel for $Pe^* = 3$ with $P = 2$ (top) and $Pe^* = 6$ with $P = 4$ (bottom). In both cases $P_{SVV} = 0$ is used. The thin dashed parabolas on the right-hand side plots show the regular (second-order) diffusion behaviour for each Pe^* .

the underlying parabolic curves related to each diffusion eigencurve are different since their associated values of Pe^* are different.

Another inconvenience of the traditional SVV operator is that for a given discretization order P , the eigencurves obtained with a prescribed value of Pe^* are only valid for the mesh spacing associated with such Pe^* . In other words, the mesh spacing h in the normalized horizontal axis of dispersion–diffusion plots is simply a scaling parameter, not a variable. For instance, considering a single diffusion plot, the SVV dissipation at kh/P is not the same as at $k'h'/P$ when $k'h' = kh$ but $h' \neq h$. This is because when h changes, so does Pe^* , and thus a different eigencurve must be consulted. As a result, in the traditional SVV approach, an eigencurve obtained for a single Pe^* provides very little information since the use of variable mesh spacing is unavoidable for practical applications. Moreover, in regions of either very small or very large mesh spacing h , SVV will eventually introduce potentially undesirable non-smooth features in the solution, as happened in the case of regular diffusion when $Pe^* \rightarrow 0$ or $Pe^* \rightarrow \infty$, recall Fig. 7. In fact, CG-SVV eigencurves with irregular features have been found easily after some experimentation and this issue seems not to be related with SVV in itself, but with the CG formulation when it comes to the discretization of viscous operators with either very low or very high values of Pe^* .

3.3. Towards more reliable SVV operators

We now propose a modification to the traditional SVV operator that not only bypasses all the issues discussed in the previous section, but also allows for the design of SVV operators that are more generally applicable. The main idea is to make the base SVV magnitude proportional to both the advection speed and mesh spacing, using $\mu = \mu_0 ah/P$. For general problems and discretizations, P would be the polynomial order used in each element (e.g. in case P -adaptation is employed), h would be a local mesh length, and a would be a measure of the advection speed within each element. Note that this implicitly makes $Pe^* = ah/\mu_0 P$ independent of a , h and P , more precisely a constant, $Pe^* = \mu_0^{-1}$. SVV characteristics will then be solely dependent on μ_0 , P , and on the kernel entries \hat{Q}_k . This approach is advantageous if one wishes to design an SVV kernel based on a fixed value of Pe^* to be used regardless of either advection speed or mesh variations.

Following the proposed approach, we now focus on the exponential kernel-based SVV operator and discuss its suitability for high-order discretizations. The variation of the exponential kernel with its mode index k can be appreciated more clearly by rewriting Eq. (46) as

$$\hat{Q}_k = \exp \left[-\frac{(\hat{k} - 1)^2}{(\hat{k} - P_{SVV}/P)^2} \right], \text{ for } \hat{k} > \frac{P_{SVV}}{P}, \quad (47)$$

where $\hat{k} = k/P$. We stress that here k is a modal index rather than a wavenumber, recall Sec. 3.1. The shapes assumed by \hat{Q}_k for $P_{SVV} = 1$ and $P_{SVV} = \sqrt{P}$ are shown in Fig. 9 for different polynomial orders, $P = 2, \dots, 7$. Both choices (fixed or variable P_{SVV}) are often used in the literature. In any case, kernel shapes can be seen to vary according the discretization order employed and essentially introduce more dissipation as P is increased. The asymptotic shape approached as $P \rightarrow \infty$ is shown as the dashed (leftmost) curves in Fig. 9 and is the same in both cases. This is also the kernel shape obtained for $P_{SVV} = 0$, in which case \hat{Q}_k becomes independent of P .

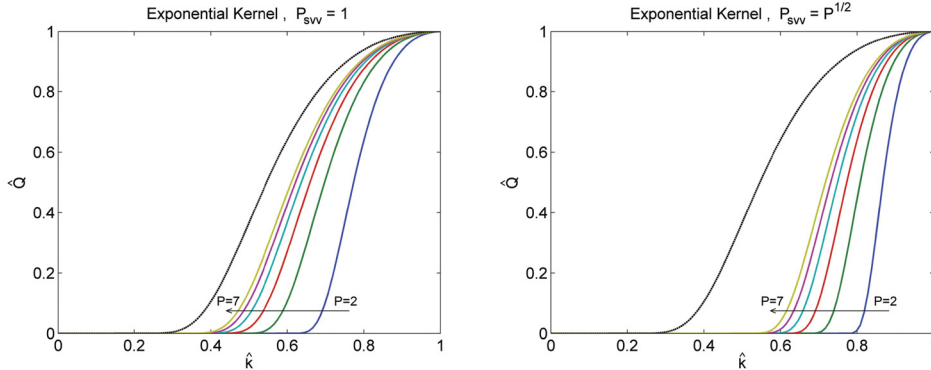


Fig. 9. Shapes assumed by the exponential kernel \hat{Q} for $P_{SVV} = 1$ (left) and $P_{SVV} = \sqrt{P}$ (right) for different polynomial orders P . The asymptotic shape approached as $P \rightarrow \infty$, shown as the dashed (leftmost) curve, is the same in both cases and correspond to the shape of \hat{Q} for $P_{SVV} = 0$.

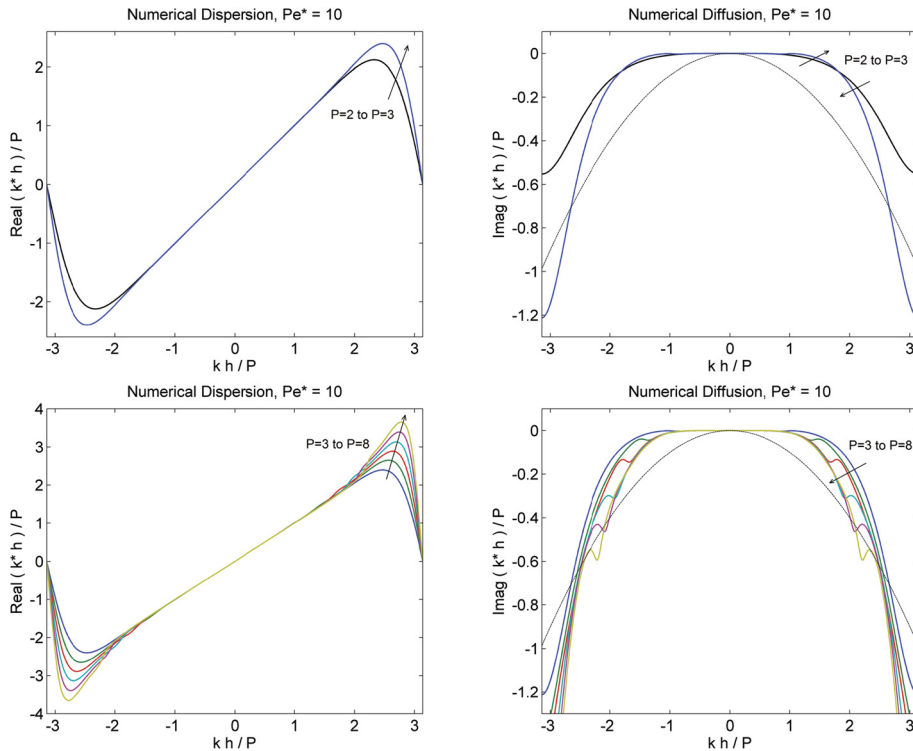


Fig. 10. Dispersion–diffusion curves for the SVV operator based on the exponential kernel (with $P_{SVV} = 0$) when $Pe^* = 10$, for $P = 2$ and 3 (top) and for $P = 3$ to 8 (bottom). Thin dashed parabolas on the diffusion plots show the regular (second-order) diffusion behaviour for $Pe^* = 10$.

The dispersion–diffusion characteristics of the SVV operator based on the exponential kernel with $P_{SVV} = 0$ are shown in Fig. 10 when $Pe^* = 10$, first for $P = 2$ and 3 and then for $P = 3$ to 8. These graphs show an undesirable feature of the exponential kernel, namely, that as P increases, “spurious” oscillations appear on the eigencurves. This behaviour is typical of the limit $Pe^* \rightarrow \infty$, recall Fig. 7, suggesting that the overall amount of viscosity introduced by the exponential kernel should be higher. Note that using $P_{SVV} = 0$ yields already the kernel shape which provides the highest levels of dissipation. Increasing P_{SVV} will only confine the viscous effects to the highest modes, thus making the situation worse. It was verified that using $P_{SVV} \propto P$ or $P_{SVV} = \sqrt{P}$ can be equally detrimental, probably for the same reason, as expected from Fig. 9 (right-hand side plot).

Increasing μ_0 can delay the oscillations until higher values of P , as shown in Fig. 11, where $Pe^* = 5$. However, another shortcoming remains: as P increases, diffusion curves are drawn inwards thus introducing more dissipation at the smaller wavenumbers. This is undesirable because SVV dissipation should begin to act at increasingly higher wavenumbers as P is increased since discretizations of higher order are expected to have a superior resolution power per degree of freedom (DOF), as is the case for the DG scheme [9].

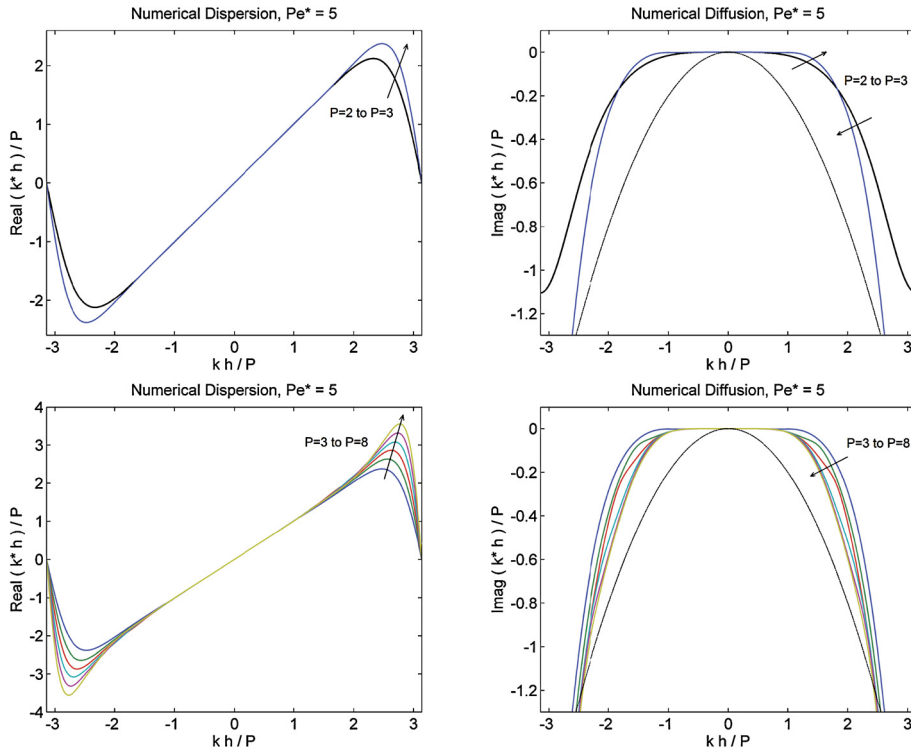


Fig. 11. Dispersion–diffusion curves for the SVV operator based on the exponential kernel (with $P_{SVV} = 0$) when $Pe^* = 5$, for $P = 2$ and 3 (top) and for $P = 3$ to 8 (bottom). Thin dashed parabolas on the diffusion plots show the regular (second-order) diffusion behaviour for $Pe^* = 5$.

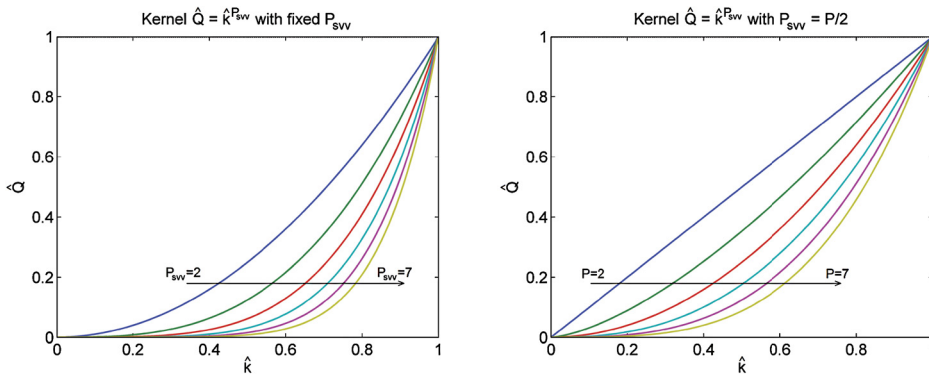


Fig. 12. Shapes assumed by the power kernel $\hat{Q}_k = \hat{k}^{P_{SVV}}$ for increasing values of P_{SVV} (left) and for $P_{SVV} = P/2$ with increasing values of P (right).

To avoid these shortcomings, a new kernel function is proposed which is given by

$$\hat{Q}_k = (k/P)^{P_{SVV}} = \hat{k}^{P_{SVV}}, \text{ for } 0 \leq \hat{k} \leq 1. \tag{48}$$

Note that this “power” kernel does not depend explicitly on P , but only on \hat{k} and P_{SVV} . Moreover, here P_{SVV} is not an activation threshold, but has a similar effect in terms of confining the viscous effects to the highest modes. This effect is shown in the left-hand side plot of Fig. 12, where the shape of the power kernel is depicted for different values of P_{SVV} .

Particularly desirable characteristics were found with the power kernel function when using $P_{SVV} \propto P$. Kernel shapes obtained with $P_{SVV} = P/2$ are shown for increasing values of P in the right-hand side graph of Fig. 12. By doing this, the viscous effects become increasingly confined to higher modes as P grows, contrary to what happens with the exponential

kernel (see Fig. 9), and at the same time a non-zero (though small) amount of dissipation is always provided for the first modes. These two features are believed to be respectively the key to avoid both the “drawing inwards” behaviour and spurious oscillations. Dispersion–diffusion eigencurves obtained with the power kernel with $P_{SVV} = P/2$ when $Pe^* = 2$ are shown in Fig. 13 for polynomial orders $P = 2, \dots, 8$.

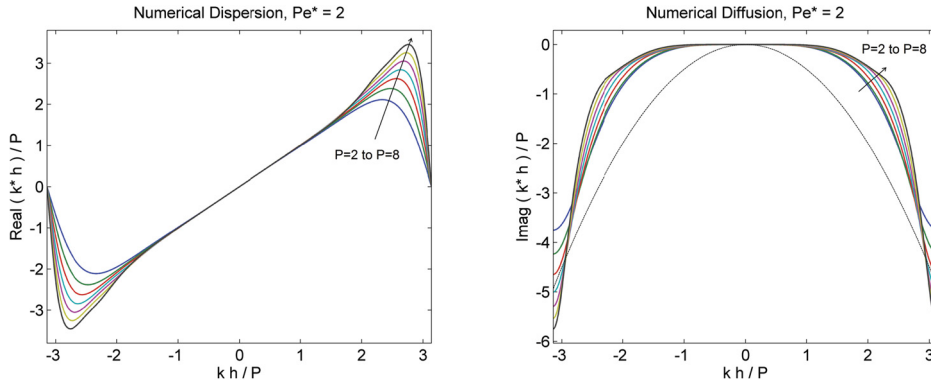


Fig. 13. Dispersion–diffusion curves for the SVV operator based on the proposed power kernel with $P_{SVV} = P/2$ for $Pe^* = 2$. The thin dashed parabola on the diffusion plot shows the regular (second-order) diffusion behaviour for $Pe^* = 2$.

We note that the power kernel would mimic the effect of hyperviscosity if applied directly in Fourier space, see Eq. (36). When however applied through a polynomial (hierarchical) setting, the resulting dissipation in Fourier space follows the same trends yielded by traditional kernel functions, as shown in Fig. 13. We also note that the power kernel function will always affect all the polynomial modes above $\hat{k} = 0$, even though this effect becomes very small for the lower-order modes when P is increased (Fig. 12). A detailed discussion on whether this feature might affect typical spectral properties achieved via P refinement, such as exponential convergence, is provided in the Appendix. Basically, we found that the SVV operator based on the power kernel with fixed P_{SVV} will exhibit algebraic decay at large values of P , whereas when P_{SVV} is made proportional to P , say as $P_{SVV} = P/2$, the magnitude of the SVV operator will decay slightly faster than exponentially. The latter approach is therefore superior and preferable.

4. Upwinding and SVV-based stabilization

As discussed in Sec. 3.2, the mesh spacing h used in the normalized horizontal axis of dispersion–diffusion plots is simply a scaling parameter, not actually a variable, in the traditional SVV approach. This causes two wavenumbers at different mesh regions where the supporting number of points per wavelength is the same (i.e. $k_1 h_1 / P = k_2 h_2 / P$) to experience distinct levels of SVV dissipation due to a Péclet number difference. On the other hand, dissipation levels peculiar to spectral/ h/p schemes with upwind-based stabilization are observed to scale naturally with the local mesh resolution, see [3–5,9]. This is exactly what is achieved with the SVV approach proposed here, where the Péclet number is held constant and so the dissipation is an actual function of kh for each P . In this sense, the dissipation characteristics of the advocated CG-SVV approach can be considered to be dimensionally equivalent to those obtained through upwinding in a DG setting, for instance.

A comparison is now carried out between the (full) upwind DG scheme and the proposed CG-SVV method with the power kernel given in Eq. (48). The main quantity considered in this comparison is the extent of the wavenumber region where numerical errors are negligible. This quantity is here estimated by the ‘1% rule’ introduced in [9], as follows. By expressing the modified wavenumber in the form $k^* = k_R^* + ik_I^*$, a propagating wave (of wavenumber k) is represented as

$$u \propto \exp[i(kx - w^*t)] = \exp(ak_I^*t) \exp[i(kx - ak_R^*t)], \tag{49}$$

where the relation $w^* = ak^*$ was used. Hence, regarding the wave’s amplitude, one has

$$|u| \propto \exp(ak_I^*t) = \exp(k_I^* \bar{h} t / \tau), \tag{50}$$

in which $\tau = \bar{h}/a$ and $\bar{h} = h/(P + 1)$. Since \bar{h} is the length measure of one DOF in both CG and DG settings, τ is the time it takes for a signal to cross a single DOF. Therefore, according to Eq. (50), for each $\Delta t = \tau$ passed, the magnitude of the propagating wave is multiplied by $\exp(k_I^* \bar{h})$, and so this quantity can be regarded as a *damping factor per DOF crossed*.

As an example, for a damping factor of 99%, the value of $k_I^* \bar{h}$ would be $\ln(0.99) \approx -0.01$. Although somewhat arbitrary, this value has been tested against one-dimensional turbulence simulations [9] and verified to be a very good measure of propagation accuracy. The 1% rule therefore consists in finding the wavenumber k for which $k_I^* \bar{h} = \ln(0.99)$. Since the natural normalization of \bar{k} is different for CG and DG, we here primarily compare values of kh given by the 1% rule, for each polynomial order P , as a measure of resolution power per element rather than per DOF. Nevertheless, the associated number of DOFs per wavelength, $2\pi / (kh)_{1\%}$, is also provided in the comparisons for reference.

Now, the viscosity parameter μ_0 chosen for the SVV operator (recall that $\mu = \mu_0 ah/P$ and so $Pe^* = \mu_0^{-1}$) should not be reduced to the point of inducing very large values of $(kh)_{1\%}$ for the diffusion curves at the cost of a vanishing overall dissipation. Therefore, for a fair comparison, μ_0 is chosen so as to provide the same damping level per element, $k_1^* h$, of the full upwind DG scheme for the smallest captured scales, i.e. at $\bar{k} = \pi$. The remaining parameter defining the SVV operator is the value of P_{SVV} from the power kernel, see Eq. (48), which is allowed to vary so as to maximize the effective resolution measure adopted, $(kh)_{1\%}$.

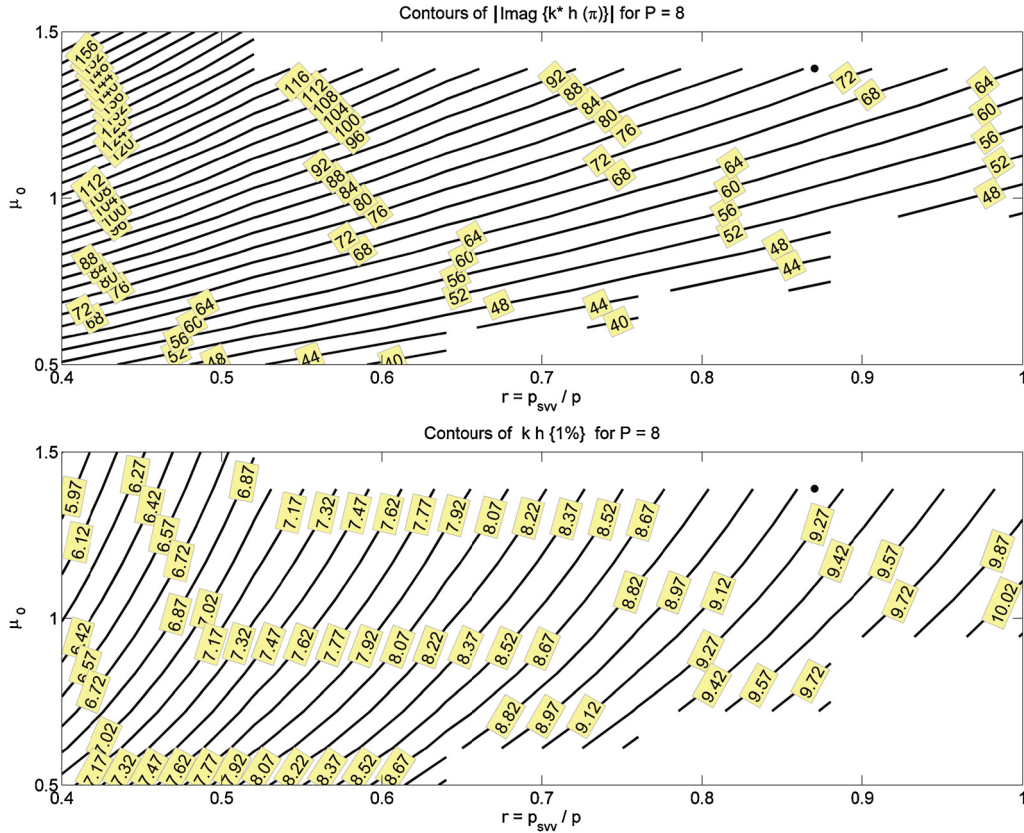


Fig. 14. Contours of $(k_1^*h)_\pi$ (top) and $(kh)_{1\%}$ (bottom) for the proposed SVV operator and power kernel for $P = 8$ and different values of μ_0 and $r = P_{SVV}/P$. The dot on the upper-right corner of the graphs corresponds to the maximum value of $(kh)_{1\%}$ along the curve $(k_1^*h)_\pi = (k_1^*h)_\pi^{DG}$.

The optimization procedure described above is illustrated in Fig. 14 for the case $P = 8$. The top and bottom graphs display contour values of $(k_1^*h)_\pi$ and $(kh)_{1\%}$, respectively, within the ranges $0.5 < \mu_0 < 1.5$ and $0.4 < r < 1.0$, where $r = P_{SVV}/P$. The dot on the upper-right corner of the graphs corresponds to the maximum value of $(kh)_{1\%}$ along the curve $(k_1^*h)_\pi = -75.06$, which is the reference DG damping level (per element) for $P = 8$. An algorithm based on the total variation of the eigencurves was employed to avoid the irregular behaviours observed when $Pe^* \rightarrow 0$ or $Pe^* \rightarrow \infty$. The blank regions in the contour plots represent dispersion–diffusion curves with oscillation levels above a certain threshold. The procedure was carried out for $P = 2, \dots, 8$ and the values of r and μ_0 leading to the optimized values of $(kh)_{1\%}$ are given in Table 1 for each polynomial order. We note that case $P = 2$ had its value of $(kh)_{1\%}$ practically unchanged along the relevant dissipation curve for a wide range of values of r , and so the set of parameters $(r, \mu_0) = (1.00, 1.58)$ was arbitrarily chosen as a representative of this range.

Table 1
Optimal parameters for the proposed SVV operator and kernel function.

P	2	3	4	5	6	7	8
r	1.00	2.87	2.45	2.07	1.31	1.02	0.87
μ_0	1.58	13.46	7.36	4.87	2.12	1.58	1.39

A graphical comparison between the eigencurves of the full upwind DG method (from [9]) and those of the CG-SVV scheme with the parameters of Table 1 is shown in Fig. 15. Effective resolution estimates for the two discretizations are compared in Table 2. The second and third columns give the estimates of resolution power per element obtained from the 1% rule for each P . The maximum wavenumber within the range of negligible numerical error can be evaluated from

Table 2

Effective resolution estimates for DG and CG-SVV for the same maximum dissipation.

P	$(kh)_{1\%}^{DG}$	$(kh)_{1\%}^{CG}$	$2\pi / (k\tilde{h})_{1\%}^{DG}$	$2\pi / (k\tilde{h})_{1\%}^{CG}$	$ k_j^* h _{,\pi}$	$\exp(k_j^* \tilde{h})_{,\pi}$
2	2.616	1.518	7.205	12.421	11.85	1.93×10^{-2}
3	4.330	3.142	5.804	8.000	19.16	8.31×10^{-3}
4	6.164	4.377	5.097	7.177	27.85	3.81×10^{-3}
5	8.071	5.599	4.671	6.733	37.92	1.80×10^{-3}
6	10.027	6.841	4.386	6.429	49.07	9.03×10^{-4}
7	12.018	7.989	4.183	6.292	60.80	5.00×10^{-4}
8	14.035	9.181	4.029	6.159	75.06	2.39×10^{-4}

such values of $(kh)_{1\%}$ for any hp setting. The next two columns compare the associated number of DOFs per wavelength for each scheme. Clearly, both discretizations achieve a consistent increase in resolution power per DOF for increasing polynomial orders. The last two columns respectively show the reference DG dissipation levels per element used for the SVV optimizations and the related damping factors per DOF.

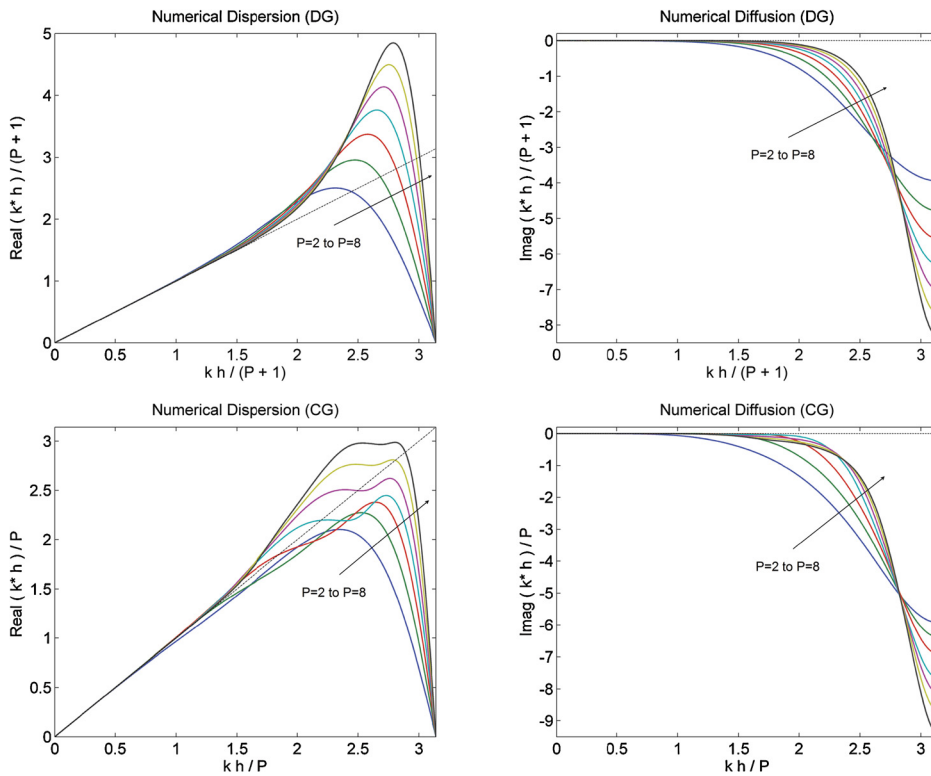


Fig. 15. Dispersion and diffusion curves for full upwind DG (top) and the optimized CG-SVV scheme (bottom) for $P = 2, \dots, 8$. Thin dashed lines represent the exact behaviour for linear advection.

The data summarized in Table 2 shows that full upwind DG and the proposed CG-SVV scheme follow the same tendency as the polynomial order is increased, but that DG has a higher resolution power per DOF. However, it should be recognized that the optimization carried out for the SVV operator was based on the (simple) power kernel suggested and that improved CG-SVV characteristics can still be pursued via different, more sophisticated kernel functions with the aid of optimization algorithms. Moreover, while DG characteristics (such as maximum dissipation) are somewhat restricted by the choice of an upwind numerical flux, the CG-SVV scheme is more flexible due to the larger number of SVV control parameters. Depending on the simulation considered and polynomial order used, DG dissipation levels are likely to be either too weak or stronger than necessary, whereas SVV could be adjusted to provide higher dissipation levels or an improved resolution power through a reduced maximum dissipation.

5. Conclusion

This study assessed the spectral/ hp continuous Galerkin (CG) formulation through the linear dispersion–diffusion analysis framework. The discretization of the advection–diffusion equation was addressed first and the role of primary and secondary eigencurves was discussed. Those have been verified to behave in agreement with the perspective introduced

in [9], by which secondary eigencurves peculiar to spectral/*hp* methods are perceived as replications of the primary one. Potentially undesirable non-smooth features have been observed on primary dispersion and diffusion curves for problems strongly dominated by either convection or diffusion. These have been found mostly at moderately high wavenumbers, indicating that high-order spectral/*hp* CG discretizations might be unsuited for under-resolved simulations of either advection or diffusion dominated problems.

Subsequently, the spectral vanishing viscosity (SVV) technique was analysed and, owing to a dependency of the traditional SVV operator on the Péclet number, the standard CG-SVV formulation was again found to feature non-smooth characteristics when convection is much stronger than dissipation or vice-versa. A new approach has been proposed where the base SVV magnitude is made locally proportional to both the advection speed and the mesh spacing. This way, the Péclet number is held constant globally and SVV effects are kept close to their design point. In addition, a “power kernel” function has been devised for the advocated SVV operator to provide a consistent increase in resolution power (per degree of freedom) when the polynomial order is increased – a feature not naturally achieved through the widely used “exponential kernel” introduced in [20]. We note however that for non-linear problems where the advection speed is solution dependent, the proposed SVV operator will also be non-linear and thus certain implementation difficulties are likely to appear. In such cases, reference values for the advection speed could be used in each element, for example.

Finally, the dissipation characteristics of the proposed SVV operator have been discussed and verified to be dimensionally equivalent to those obtained with upwind numerical fluxes. The CG formulation based on the suggested SVV operator and kernel function has been compared with the full upwind DG scheme in terms of effective resolution power (as measured by the extent of the wavenumber range where numerical errors are negligible) according to the 1% rule introduced in [9]. The DG scheme has been found to have a moderately higher resolution power for the same dissipation levels. However, the results here obtained for CG were based on the power kernel and thus can only be regarded as ‘locally optimal’. Improved CG-SVV characteristics can still be pursued via different kernel functions with the aid of optimization algorithms. Also, resolution power is not all that matters in under-resolved simulations. Sometimes it might be desirable to increase the overall dissipation simply to improve robustness, or to manipulate diffusion curves in order to mimic the spectral behaviour of some subgrid-scale model [13,15,16]. Due to its larger number of control parameters, SVV can be more generally adjusted (when compared to DG) to provide the desired dissipation levels for complex problems, such as in transition and turbulence simulations.

Acknowledgements

RCM would like to acknowledge funding under the Brazilian Science without Borders scheme. SJS would like to acknowledge support as Royal Academy of Engineering Research Chair. JP and SJS additionally acknowledge support from the Engineering and Physical Sciences Research Council (EPSRC) under grant EP/L000407/1.

Appendix A

This section is devoted to a discussion of convergence properties of the SVV operator based on the “power” kernel proposed in Sec. 3.3, see Eq. (48). We start by noting that, in a pure spectral formulation, the effect of SVV can be directly analysed by inserting Eq. (48) into Eq. (36), which yields

$$\mu \frac{\partial}{\partial x} \left(\mathcal{Q} \star \frac{\partial u}{\partial x} \right) = -\mu / P^{P_{SVV}} \sum_k k^{P_{SVV}+2} \hat{u}_k \exp(ikx), \quad (51)$$

whereby SVV formally mimics a hyperviscous operator of order $P_{SVV} + 2$. We acknowledge, however, that the operator’s behaviour for spectral/*hp* methods is expected to be somewhat different since spectral/*hp* discretizations are based on polynomials rather than on complex exponential functions. Nonetheless, it is hoped that some of the properties (convergence properties, in particular) observed for pure spectral formulations are maintained for spectral/*hp* methods, as in fact happens with traditional SVV approaches.

From Eq. (51) one can estimate the magnitude of the SVV operator at a given wavenumber k as

$$\|SVV_k(P)\| \propto k^{P_{SVV}+2} / P^{P_{SVV}-1}, \quad (52)$$

since typically $\mu \propto 1/P$. As a result, for P_{SVV} fixed, one has

$$\|SVV_k(P)\| \propto 1/P^{P_{SVV}-1} \implies \log \|SVV_k(P)\| \propto -(P_{SVV} - 1) \log P + \text{const}, \quad (53)$$

and for P_{SVV} varying with P , say as $P_{SVV} = P/n$,

$$\|SVV_k(P)\| \propto k^{P/n+2} / P^{P/n-1} \implies \log \|SVV_k(P)\| \propto -P/n \log(P/k) + \text{const}, \quad (54)$$

where the last result is an approximation which assumes P large. The above results indicate that the effect of the power kernel-based SVV operator should decay algebraically via P refinement for P_{SVV} fixed, whereas for $P_{SVV} = P/n$ the decay

can be faster than exponential. Moreover, higher rates of decay could be obtained with larger values of P_{SVV} in Eq. (53) and smaller values of n in Eq. (54).

We now present some numerical results to substantiate the convergence estimates above. The Kovaszny flow [22] which represents a steady, laminar flow behind a two-dimensional grid was used to test how the power kernel-based SVV operator affects the spectral convergence properties of the continuous Galerkin formulation. This test case has been used in previous works [13,14] to assess the error introduced by traditional SVV operators as applied to spectral/hp methods. A version of the analytical solution which is suitable for numerical tests can be found in [7] (see chapter 9) and is given by

$$u = 1 - e^{\lambda x} \cos(2\pi y), \quad v = \frac{\lambda}{2\pi} e^{\lambda x} \sin(2\pi y), \quad p = \frac{1}{2}(1 - e^{2\lambda x}), \tag{55}$$

where u and v represent the x and y velocity components, p is the pressure and $\lambda = (2\nu)^{-1} - [(2\nu)^{-2} + 4\pi^2]^{1/2}$, in which ν stands for the fluid’s kinematic viscosity. The value $\nu = 1/400$ has been chosen here and found to be sufficiently small so as not to suppress the effects of the SVV in the numerical solution.

From the discussions in Sec. 3.3, the value $Pe^* = 2$ has been adopted for the tests of the power kernel (see e.g. Fig. 13) and the value $Pe^* = 5$ has been used for the tests conducted with the exponential kernel, which will be useful for comparison. We note that these values represent a 2.5 times stronger base viscosity $\mu = a\bar{h}/Pe^*$ for the power kernel-based SVV operator. Since from the analytical solution the average of u and v over the plane are respectively one and zero, the constant value $a = 1$ has been adopted globally in the test cases. The Kovaszny flow was solved in the rectangular domain $[-1/2, 3/2] \times [-1/2, 3/2]$ in an equispaced grid consisting of 16 square-shaped elements of side $h = 1/2$. Dirichlet boundary conditions based on the analytical solution have been imposed where appropriate. The incompressible Navier–Stokes solver encapsulated within spectral/hp element code Nektar++ [23] was used for the test cases.

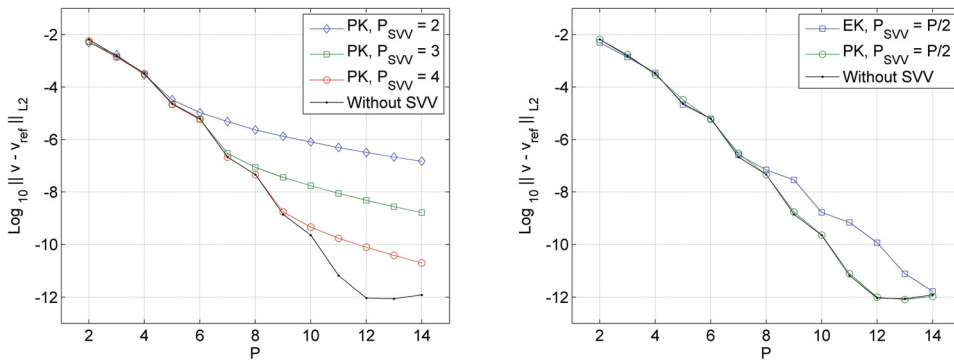


Fig. 16. Log-linear convergence plots of the error (L^2 norm) on the y velocity component. Left: results without SVV are compared with those obtained with the power kernel (PK) for different given values of P_{SVV} . Right: results obtained with the exponential kernel (EK) are compared with those of the power kernel, both using $P_{SVV} = P/2$.

Fig. 16 displays the convergence of the error (L^2 norm) on the y velocity component, v , which can be measured easily by comparison with the analytical solution. The convergence curves based on u or p (not shown) presented very similar trends and were just a bit more wiggly. Such results clearly support the convergence estimates given in Eqs. (53)–(54). In particular, they show that the power kernel with varying P_{SVV} is to be preferred over its counterpart based on a fixed P_{SVV} value, since the error introduced by this latter approach will eventually surpass the baseline error of the CG discretization as the polynomial order is increased. Also, when using $P_{SVV} = P/2$, the comparison with the exponential kernel indicates that introducing a small amount of dissipation at the lower-order modes is not necessarily worse than introducing none, which by construction is the case for the exponential kernel tested.

Finally, the kernel functions employed in the two-dimensional discretization were, for the power kernel,

$$\hat{Q}_{i,j} = \left(\frac{i}{P}\right)^{P_{SVV}} \left(\frac{j}{P}\right)^{P_{SVV}} \quad \text{for } 0 \leq i, j \leq P, \tag{56}$$

and, for the exponential kernel which becomes non-zero only above P_{SVV} ,

$$\hat{Q}_{i,j} = \exp\left[-\frac{(i-P)^2}{(i-P_{SVV})^2}\right] \exp\left[-\frac{(j-P)^2}{(j-P_{SVV})^2}\right] \quad \text{for } i, j > P_{SVV}, \tag{57}$$

where i, j are used to indicate the index of the polynomial mode in a tensor-product Legendre orthogonal basis spanning the polynomial space of degree P , see [7].

References

- [1] P.E. Vincent, A. Jameson, Facilitating the adoption of unstructured high-order methods amongst a wider community of fluid dynamicists, *Math. Model. Nat. Phenom.* 6 (3) (2011) 97–140.
- [2] F.Q. Hu, M.Y. Hussaini, P. Rasetarinera, An analysis of the discontinuous Galerkin method for wave propagation problems, *J. Comput. Phys.* 151 (2) (1999) 921–946.
- [3] K. Van den Abeele, T. Broeckhoven, C. Lacor, Dispersion and dissipation properties of the 1D spectral volume method and application to a p-multigrid algorithm, *J. Comput. Phys.* 224 (2) (2007) 616–636.
- [4] K. Van den Abeele, C. Lacor, Z.J. Wang, On the stability and accuracy of the spectral difference method, *J. Sci. Comput.* 37 (2) (2008) 162–188.
- [5] P.E. Vincent, P. Castonguay, A. Jameson, Insights from von Neumann analysis of high-order flux reconstruction schemes, *J. Comput. Phys.* 230 (22) (2011) 8134–8154.
- [6] S.J. Sherwin, Dispersion analysis of the continuous and discontinuous Galerkin formulations, in: B. Cockburn, G.E. Karniadakis, C.W. Shu (Eds.), *Discontinuous Galerkin Methods: Theory, Computation and Applications*, Springer, 2000, pp. 425–431.
- [7] G.E. Karniadakis, S.J. Sherwin, *Spectral/hp Element Methods for Computational Fluid Dynamics*, 2nd edition, Oxford University Press, 2005.
- [8] P.M. Gresho, R.L. Sani, *Incompressible Flow and the Finite Element Method. Vol. 1: Advection–Diffusion*, John Wiley and Sons, 1998.
- [9] R.C. Moura, S.J. Sherwin, J. Peiró, Linear dispersion–diffusion analysis and its application to under-resolved turbulence simulations using discontinuous Galerkin spectral/hp methods, *J. Comput. Phys.* 298 (2015) 695–710.
- [10] E. Tadmor, Convergence of spectral methods for nonlinear conservation laws, *SIAM J. Numer. Anal.* 26 (1) (1989) 30–44.
- [11] Ø. Andreassen, I. Lie, C.E. Wasberg, The spectral viscosity method applied to simulation of waves in a stratified atmosphere, *J. Comput. Phys.* 110 (2) (1994) 257–273.
- [12] S.M.O. Kaber, A Legendre pseudospectral viscosity method, *J. Comput. Phys.* 128 (1) (1996) 165–180.
- [13] G.S. Karamanos, G.E. Karniadakis, A spectral vanishing viscosity method for large-eddy simulations, *J. Comput. Phys.* 163 (1) (2000) 22–50.
- [14] R.M. Kirby, S.J. Sherwin, Stabilisation of spectral/hp element methods through spectral vanishing viscosity: application to fluid mechanics modelling, *Comput. Methods Appl. Mech. Eng.* 195 (23) (2006) 3128–3144.
- [15] R.M. Kirby, G.E. Karniadakis, Coarse resolution turbulence simulations with spectral vanishing viscosity–large-eddy simulations (SVV–LES), *J. Fluids Eng.* 124 (4) (2002) 886–891.
- [16] R. Pasquetti, Spectral vanishing viscosity method for LES: sensitivity to the SVV control parameters, *J. Turbul.* 6 (12) (2005).
- [17] R. Pasquetti, Spectral vanishing viscosity method for large-eddy simulation of turbulent flows, *J. Sci. Comput.* 27 (1–3) (2006) 365–375.
- [18] M. Minguez, R. Pasquetti, E. Serre, High-order large-eddy simulation of flow over the ‘Ahmed body’ car model, *Phys. Fluids* 20 (9) (2008) 095101.
- [19] K. Koyal, J. Stiller, H.M. Blackburn, Adapting the spectral vanishing viscosity method for large-eddy simulations in cylindrical configurations, *J. Comput. Phys.* 231 (8) (2012) 3389–3405.
- [20] Y. Maday, S.M.O. Kaber, E. Tadmor, Legendre pseudospectral viscosity method for nonlinear conservation laws, *SIAM J. Numer. Anal.* 30 (2) (1993) 321–342.
- [21] C. Xu, R. Pasquetti, Stabilized spectral element computations of high Reynolds number incompressible flows, *J. Comput. Phys.* 196 (2) (2004) 680–704.
- [22] L.I.G. Kovasznay, Laminar flow behind a two-dimensional grid, *Math. Proc. Camb. Philos. Soc.* 44 (1948) 58–62.
- [23] C.D. Cantwell, D. Moxey, A. Comerford, A. Bolis, G. Rocco, G. Mengaldo, D. De Grazia, S. Yakovlev, J. Lombard, D. Ekelschot, B. Jordi, H. Xu, Y. Mohamied, C. Eskilsson, B. Nelson, P. Vos, C. Biotto, R.M. Kirby, S.J. Sherwin, Nektar++: an open-source spectral/hp element framework, *Comput. Phys. Commun.* 192 (2015) 205–219.